Monthly Notices of the ROYAL ASTRONOMICAL SOCIETY

MNRAS **511,** 120–138 (2022) https://doi.org/10.1093/mnras/stab3728
Advance Access publication 2021 December 23

No strong dependence of Lyman continuum leakage on physical properties of star-forming galaxies at $3.1 \lesssim z \lesssim 3.5$

A. Saxena [1★] L. Pentericci,[2] R. S. Ellis,[1] L. Guaita,[3] A. Calabrò,[2] D. Schaerer,[4,5] E. Vanzella,[6] R. Amorín,[7,8] M. Bolzonella [9] M. Castellano,[2] F. Fontanot [10,11] N. P. Hathi [12] P. Hibon [13] M. Llerena [8] F. Mannucci [14] A. Saldana-Lopez [4] M. Talia[15] and G. Zamorani[9]

[1]*Department of Physics and Astronomy, University College London, Gower Street, London WC1E 6BT, UK*
[2]*INAF – Osservatorio Astronomico di Roma, via Frascati 33, I-00078 Monteporzio Catone, Italy*
[3]*Departamento de Ciencias Fisicas, Universidad Andres Bello, Fernandez Concha 700, Las Condes, Santiago, Chile*
[4]*Observatoire de Genève, Département d'Astronomie, Université de Genève, 51 Chemin Pegasi, CH-1290 Versoix, Switzerland*
[5]*CNRS, IRAP, 14 avenue E. Belin, F-31400 Toulouse, France*
[6]*INAF – Osservatorio Astronomico di Bologna, Via P. Gobetti 93/3, I-40129 Bologna, Italy*
[7]*Instituto de Investigación Multidisciplinar en Ciencia y Tecnología, Universidad de La Serena, Raúl Bitrán, 1305 La Serena, Chile*
[8]*Departamento de Física y Astronomía, Universidad de La Serena, Av. Juan Cisternas 1200 Norte, La Serena, Chile*
[9]*INAF – Osservatorio di Astrofisica e Scienza dello Spazio di Bologna, via Piero Gobetti 93/3, I-40129 Bologna, Italy*
[10]*INAF – Astronomical Observatory of Trieste, Via G.B. Tiepolo 11, I-34143 Trieste, Italy*
[11]*IFPU – Institute for Fundamental Physics of the Universe, Via Beirut 2, I-34151 Trieste, Italy*
[12]*Space Telescope Science Institute, 3700 San Martin Drive, Baltimore, MD 21218, USA*
[13]*European Southern Observatory (ESO), Alonso de Córdova 3107, Vitacura, Casilla 19001, Santiago, Chile*
[14]*INAF – Osservatorio Astrofisico di Arcetri, Largo E. Fermi 5, I-50125 Firenze, Italy*
[15]*University of Bologna – Department of Physics and Astronomy 'Augusto Righi' (DIFA), Via Gobetti 93/2, I-40129 Bologna, Italy*

Accepted 2021 December 19. Received 2021 November 23; in original form 2021 September 9

ABSTRACT

We present Lyman continuum (LyC) radiation escape fraction ($f_{\rm esc}$) measurements for 183 spectroscopically confirmed star-forming galaxies in the redshift range $3.11 < z < 3.53$ in the *Chandra* Deep Field South. We use ground-based imaging to measure $f_{\rm esc}$, and use ground- and space-based photometry to derive galaxy physical properties using spectral energy distribution (SED) fitting. We additionally derive [O III] + Hβ equivalent widths (that fall in the observed K band) by including nebular emission in SED fitting. After removing foreground contaminants, we report the discovery of 11 new candidate LyC leakers at $\gtrsim 2\sigma$ level, with $f_{\rm esc}$ in the range 0.14−0.85. From non-detections, we place 1σ upper limits of $f_{\rm esc} < 0.12$, where the Lyman-break selected galaxies have $f_{\rm esc} < 0.11$ and 'blindly' discovered galaxies with no prior photometric selection have $f_{\rm esc} < 0.13$. We find a slightly higher 1σ limit of $f_{\rm esc} < 0.20$ from extreme emission line galaxies with rest-frame [O III] + Hβ equivalent widths > 300 Å. For candidate LyC leakers, we find a weak negative correlation between $f_{\rm esc}$ and galaxy stellar masses, no correlation between $f_{\rm esc}$ and specific star-formation rates (sSFRs) and a positive correlation between $f_{\rm esc}$ and EW$_0$([O III] + Hβ). The weak/no correlations between stellar mass and sSFRs may be explained by misaligned viewing angles and/or non-coincident time-scales of starburst activity and periods of high $f_{\rm esc}$. Alternatively, escaping radiation may predominantly occur in highly localized star-forming regions, or $f_{\rm esc}$ measurements may be impacted by stochasticity of the intervening neutral medium, obscuring any global trends with galaxy properties. These hypotheses have important consequences for models of reionization.

Key words: galaxies: evolution – galaxies: high-redshift – dark ages, reionization, first stars – early Universe.

1 INTRODUCTION

Constraining when and how the intergalactic medium (IGM) in the Universe made a phase transition from neutral to completely ionized, i.e. the epoch of reionization (EoR) is an exciting challenge in observational cosmology. An important period in the evolutionary history of our Universe, EoR was likely triggered by UV photon production by the first stars, galaxies, and supermassive black holes in the Universe (Bromm & Yoshida 2011) and observations suggest that the reionization of the Universe unfolded over the redshift range $6 \lesssim z \lesssim 10$ (e.g. Planck Collaboration XIII 2016b). To understand how reionization progressed, knowledge of the intrinsic ionizing spectra of sources in the early Universe is needed, in addition to the fraction of Hydrogen-ionizing Lyman continuum (LyC; $\lambda_0 < 912$ Å) photons that actually escape into the neutral IGM driving reionization (see Dayal & Ferrara 2018, for a recent review). The rapidly increasing neutrality of the IGM at high redshifts (e.g. Inoue et al. 2014) makes

★ E-mail: aayush.saxena@ucl.ac.uk

© The Author(s) 2021.
Published by Oxford University Press on behalf of Royal Astronomical Society. This is an Open Access article distributed under the terms of the Creative Commons Attribution License (http://creativecommons.org/licenses/by/4.0/), which permits unrestricted reuse, distribution, and reproduction in any medium, provided the original work is properly cited.

Downloaded from https://academic.oup.com/mnras/article/511/1/120/6481640 by guest on 17 March 2023

it impossible to directly observe LyC photons from reionization era galaxies even with facilities like the *James Webb Space Telescope (JWST)* and therefore, the only possibility to obtain constraints on the escape fraction of LyC photons (f_{esc}) is by studying lower redshift analogues of reionization era galaxies, where escaping LyC photons are not completely absorbed by the comparatively less neutral IGM.

Assuming a constant LyC escape fraction for galaxies across the full range of UV luminosities or stellar masses, various works (Robertson et al. 2013, 2015, but see also Naidu et al. 2020) have determined that $f_{esc} \approx 10$–20 per cent is required to both reionize the Universe by $z \sim 6$ and match the Thomson optical depth of electron scattering observed in the cosmic microwave background (Planck Collaboration XIII 2016b). High-resolution zoom-in simulations of reionization era galaxies have suggested that f_{esc} could be higher in lower mass systems, as the energy and momentum ejected by supernova explosions are able to clear out channels of neutral gas more efficiently in lower mass environments, facilitating LyC photon escape (Wise et al. 2014; Trebitsch et al. 2017). Other simulations, however, have suggested a non-monotonic dependence of f_{esc} on stellar/halo mass, where f_{esc} is lower at the low mass end ($M_\star < 10^8$ M$_\odot$) due to inefficient star formation, peaks at $M_\star \sim 10^8$ M$_\odot$ and decreases again at higher masses due to dust attenuation (e.g. Ma et al. 2020).

Alternatively, a strong dependence of f_{esc} on the star-formation rate surface density may imply that higher mass galaxies ($>10^8$ M$_\odot$) at $z > 6$ may contribute > 80 per cent of the reionization photon budget and also explain the rapid conclusion of reionization (Naidu et al. 2020). Active galactic nuclei (AGNs) at $z > 6$, with a considerably higher f_{esc} on average compared to star-forming galaxies (Cristiani et al. 2016; Grazian et al. 2018; Romano et al. 2019), may also contribute to the observed rapid evolution of the IGM neutral fraction at $z > 6$ (Fontanot, Cristiani & Vanzella 2012; Giallongo et al. 2015; Trebitsch et al. 2018; Finkelstein et al. 2019; Dayal et al. 2020), and contributions to the reionization budget may be expected from low-metallicity X-ray binaries binary populations in high redshift galaxies (Madau & Fragos 2017; Schaerer, Fragos & Izotov 2019; Saxena et al. 2021).

However, no conclusive correlations between f_{esc} and stellar masses or star-formation rates have yet been identified observationally. LyC measurements presented by Izotov et al. (2021) for a sample of very low mass ($M_\star < 10^8$ M$_\odot$) galaxies at $0.30 < z < 0.45$ showed that f_{esc} does not strongly depend on the stellar mass over a broad mass range of $10^7 - 10^{10}$ M$_\odot$. Radiative transfer modelling has suggested that density-bounded H II regions within star-forming galaxies, traced by high [O III]/[O II] ratios (O32; Zackrisson, Inoue & Jensen 2013), offer ideal environments to achieve high f_{esc} values (Jaskot & Oey 2013; Nakajima & Ouchi 2014; Faisst 2016; Izotov et al. 2018a) and although spectroscopic follow-up of candidate LyC leakers at $z \sim 3$ has shown that galaxies with high f_{esc} can also show high O32 (e.g. Vanzella et al. 2016b; Nakajima et al. 2020), several other physical phenomena that do not require high f_{esc} can also lead to high O32 ratios within galaxies (e.g. Stasińska et al. 2015; Izotov, Thuan & Guseva 2017; Paalvast et al. 2018; Jaskot et al. 2019). Therefore, a high O32 does not also necessarily guarantee high f_{esc} (Izotov et al. 2018a; Naidu et al. 2018; Bassett et al. 2019; Nakajima et al. 2020).

Further, studies that have attempted to measure f_{esc} from intermediate redshift galaxies using both ground-based (e.g. Grazian et al. 2016; Guaita et al. 2016; Japelj et al. 2017; Marchi et al. 2017; Naidu et al. 2018) and space-based (e.g. Mostardi et al. 2015; Siana et al. 2015; Rutkowski et al. 2017; Fletcher et al. 2019) UV imaging have generally found low f_{esc} values ($<$ 10–20 per cent), with no clear differences in f_{esc} measured from photometrically selected Lyman break galaxies (LBGs) or galaxies selected based on strong emission lines. LyC f_{esc} measured from compact Lyman alpha emitting galaxies (LAEs), considered to be direct analogues of reionization era galaxies, have reported a higher incidence of individual LyC leakers (with $f_{esc} \gtrsim 10$ per cent; e.g. Fletcher et al. 2019), but average f_{esc} measured through stacking of non-leakers remains low (Mostardi et al. 2013; Fletcher et al. 2019; Bian & Fan 2020; Smith et al. 2020) and consistent with that derived for other types of galaxies. The candidate LyC leaking galaxies identified at $z \sim 2$–4, with $f_{esc} > 20$ per cent (e.g. de Barros et al. 2016; Shapley et al. 2016; Vanzella et al. 2016a, 2018; Bian et al. 2017; Fletcher et al. 2019; Rivera-Thorsen et al. 2019; Meštrić et al. 2020; Marques-Chaves et al. 2021), also generally occupy a broad range of stellar masses, star-formation rates, and rest-optical nebular line strengths (e.g. [O III]), showing no clear preference or dependence on either of these parameters.

To fully understand the nature of galaxies that drove reionization, thereby dictating both the spatial and temporal evolution of the neutral fraction of the IGM at $z > 6$, it is necessary to uniformly probe the dependence of f_{esc} on galaxy properties using large samples of star-forming galaxies at intermediate redshifts. To do this, a combination of accurate spectroscopic redshifts, deep rest-frame LyC data, and multiband photometry that enables reliable constraints on the spectral energy distributions (SEDs) is needed. This combination is crucial to overcome uncertainties in the measurement of both LyC f_{esc} as well as galaxy properties such as stellar masses, star-formation rates (SFRs), histories, ages, metallicities, dust attenuation, etc., which may also impact the inferred f_{esc} (Dayal & Ferrara 2018). Accurate redshifts can also minimize the uncertainties in the IGM transmission along the line of sight that can further affect the f_{esc} measurement (e.g. Bassett et al. 2021).

Therefore, in this study we construct a sample of star-forming galaxies with high quality spectroscopic redshifts at $z = 3.11$–3.53 for which deep ground-based imaging probing rest-frame LyC emission is available. Our aim is to uniformly measure LyC f_{esc} and key galaxy properties using SED fitting to explore potential correlations between them. The galaxy sample used in this study probes a range of UV luminosities, stellar masses, and star-formation rates, containing galaxies that were photometrically selected for spectroscopic follow-up based on their Lyman break, as well as blindly discovered galaxies from deep imaging-spectroscopy surveys of the sky. Each galaxy benefits from deep *Hubble Space Telescope (HST)* and *Spitzer*/IRAC imaging of their non-ionizing wavelengths, which enables highly reliable SED fitting. The redshift range of our sample is further advantageous due to the redshifted [O III] + Hβ emission lines falling in the observed *K* broadband, enabling the exploration of the connection between f_{esc} and [O III] + Hβ line strengths.

The layout of this paper is as follows. We describe the LyC imaging and the spectroscopic data sets used in this study, along with the sample selection and foreground contamination identification in Section 2. In Section 3 we describe the SED fitting procedure used to derive key physical properties for our galaxies as well as estimate [O III] + Hβ line strengths. In Section 4 we describe our LyC f_{esc} measurements and present the results for both individual galaxies as well as f_{esc} measured through stacking. We also present stacked f_{esc} measurements for subsamples of galaxies, including those for galaxies that show extremely strong [O III] + Hβ emission lines. In Section 5 we explore the dependence of f_{esc} on key galaxy properties such as stellar masses, specific star-formation rates, and [O III] + Hβ strengths for both individual f_{esc} measurements and stacks. Finally in Section 6 we discuss the implications of our results and discuss mechanisms that likely regulate f_{esc}.

Downloaded from https://academic.oup.com/mnras/article/511/1/120/6481640 by guest on 17 March 2023

Throughout this paper, we assume a ΛCDM cosmology with $\Omega_m = 0.3$ and $H_0 = 67.7$ km s^{-1} Mpc^{-1} taken from Planck Collaboration XIII (2016a), and use the AB magnitude system (Oke & Gunn 1983). All logarithms are in base 10, unless otherwise specified.

2 DATA AND SAMPLE SELECTION

In this work, we focus on the Great Observatories Origins Deep Survey-South (GOODS-S) extragalactic field,[1] which benefits from deep photometric and spectroscopic observations of galaxies from ground- and space-based observatories across a wide wavelength range, for example through the Cosmic Assembly Near-infrared Deep Extragalactic Legacy Survey (CANDELS; Grogin et al. 2011; Koekemoer et al. 2011). This field also benefits from deep narrow-band (Guaita et al. 2016) and broad-band imaging data (Nonino et al. 2009) probing rest-frame LyC wavelengths at $z \sim 3$–3.5, and deep *HST* and *Spitzer* data that enables reliable SED fitting, crucially at wavelengths redwards of the Balmer break at $z \sim 3.5$ (around 4000 Å rest-frame). We first describe the available LyC filters in this field below, followed by the spectroscopic data used in this study, possible foreground contaminant identification, and final galaxy sample creation.

2.1 LyC filters – narrow bands and *U* band

To measure LyC signal, typically measured in the rest-frame wavelength range $860 < \lambda < 912$ Å at $z > 3$, we use narrow-band imaging data from Guaita et al. (2016) and the publicly available *U*-band imaging data (Nonino et al. 2009). We briefly describe the properties of these LyC filters below.

The images from the narrow bands (NB) *NB3727* and *NB396* were first presented in Guaita et al. (2016) and we refer the readers to this paper for full details of the observations, data reduction, calibration, and other properties associated with these images. Briefly, the *NB3727* image was obtained using the MOSAIC II instrument at the Cerro Tololo Interamerican Observatory (CTIO), with the exposure time totalling to 36 h, a total coverage area of 31.5 × 31.5 arcmin^2 on the sky and 1σ detection limit of 27.38 AB. *NB3727* offers LyC coverage in the wavelength range mentioned above for redshifts $3.11 < z < 3.34$.

The *NB396* image was obtained using the WFI instrument mounted on the ESO 2.2m Telescope at La Silla, with a total exposure time of 13 h, covering a subset of the sky area encompassed by the *NB3727* image with a 1σ detection limit at 27.72 AB. *NB396* samples LyC signal in the range $3.41 < z < 3.53$.

We also use the deep *U*-band image in the GOODS-S field taken by Nonino et al. (2009) using VIMOS on the *Very Large Telescope (VLT)* covering an area of ≈630 arcmin^2 and reaching a 1σ magnitude limit of 29.78 AB. The *U*-band filter covers rest-frame LyC signal in the redshift range $3.34 < z < 3.49$. Although flux bluewards of the Lyman break is sampled for redshifts above 3.49, the declining IGM transmissivity would strongly suppress the expected flux at these shorter wavelengths (e.g. Inoue et al. 2014) and may bias the measured LyC fluxes. The transmission curves and the redshift range over which the rest-frame LyC flux is sampled by each filter are shown in Fig. 1.

Therefore, owing to the rest-frame LyC wavelength coverage offered by imaging data, the redshift range probed in this study is $3.11 < z < 3.53$. We now present the spectroscopic data within the GOODS-S/CDFS field used to construct a sample of star-forming galaxies in this redshift range.

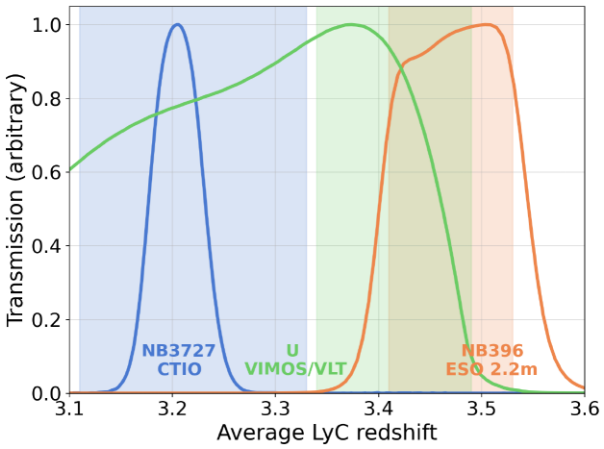


Figure 1. Filter transmission profiles of the *NB3727*, *NB396*, and the *U*-band filters used to target LyC emission in this study. The x-axis shows the redshift at the rest-frame wavelength of 886 Å, which is the mid-point wavelength of the LyC emission sampled between $860 < \lambda < 912$ Å in this study (shaded regions for each filter). More details about the filter properties and LyC redshift ranges covered are given in Section 2.1.

2.2 Spectroscopic data

2.2.1 *VANDELS*

The majority of spectra used in this study are from VANDELS – a deep VIMOS survey of the CANDELS UDS and CDFS fields – which is a recently completed ESO public spectroscopic survey carried out using the VLT. The VANDELS survey covers two well-studied extragalactic fields, the UKIDSS Ultra Deep Survey (UDS) centred around RA = 02:17:38, Dec = −05:11:55, and the Chandra Deep Field South (CDFS/GOODS-S) centred around RA = 03:32:30, Dec = −27:48:28. As mentioned earlier, we use VANDELS spectra in the CDFS/GOODS-S field in this study. The survey description and target selection can be found in McLure et al. (2018), and detailed data reduction and redshift determination steps can be found in Pentericci et al. (2018).

VANDELS spectroscopic targets were selected based on photometric redshifts (or the presence of Lyman breaks in their broad-band photometry) derived from deep ground and space-based multiband photometry. The parent spectroscopic sample included bright star-forming galaxies ($i \leq 25.0$ AB) in the range $2.4 \leq z \leq 5.5$ with 99 per cent of this subsample having specific star-formation rates (sSFR) >0.6 Gyr^{-1}, fainter Lyman-break galaxies (LBGs; $i \leq 27.5$ AB) in the redshift range $3.0 \leq z \leq 7.0$ with sSFR >0.3 Gyr^{-1} and passive galaxies with sSFR <0.1 Gyr^{-1} (McLure et al. 2018). Over the redshift range of interest for this study, the VANDELS galaxies are largely sampled from the star-forming main sequence.

The latest VANDELS data release, DR4 (Garilli et al. 2021)[2] contains spectra of ∼2100 galaxies in the redshift range $1.0 < z < 7.0$, with on-source integration times ranging from 20 to 80 h, where > 70 per cent of the targets have at least 40 h of integration time. The survey depths have been chosen so that the final spectra have high signal-to-noise ratios (SNRs), enabling detailed absorption

[1] https://www.stsci.edu/science/goods/

[2] http://vandels.inaf.it/dr4.html

Downloaded from https://academic.oup.com/mnras/article/511/1/120/6481640 by guest on 17 March 2023

and emission line studies, the study of ionizing sources using emission line ratios, the derivation of accurate metallicities, and better constraints on physical parameters such as stellar masses and star-formation rates. The spectral resolution of the final spectra is $R \sim 600$.

The spectra used in this study were reduced using the EASYLIFE data reduction pipeline (Garilli et al. 2012) and the final data products delivered by VANDELS include the extracted 1D spectra, the 2D re-sampled and sky-subtracted spectra and catalogues with physical parameters, including spectroscopic redshifts. The reliability of redshifts in the VANDELS data base is recorded using the following flags: 0 – no redshift could be assigned, 1–50 per cent probability to be correct, 2–70–80 per cent probability to be correct, 3–95–100 per cent probability to be correct, 4–100 per cent probability to be correct, and 9 – spectrum shows a single emission line. The typical accuracy of spectroscopic redshift measurements is $\sim$150 km s^{-1}. Details about the final VANDELS data products, redshift determination processes, and redshift reliability flags assignment can be found in Pentericci et al. (2018).

In the redshift range $3.11 < z < 3.53$, we identified 90 galaxies with spectroscopic flags 3 and 4, which guarantees a $>$ 95 per cent probability that the spectroscopic redshift is correct and reliable. The VANDELS team has performed aperture matched, PSF-homogenized photometry for every source identified in the CANDELS footprint in GOODS-S across available imaging data ranging from UV to NIR wavelengths (McLure et al. 2018), which we refer to as the 'master' catalogue. Accurate and homogenized photometry is essential for robust SED fitting to determine key galaxy properties and we rely on photometry from this master catalogue for this study.

Therefore, moving forward we require every source selected from other publicly available spectroscopic data that are described below to have a matched entry in the master catalogue and below we list the other publicly available data sets from which sources with reliable spectroscopic redshifts were queried.

2.2.2 *VUDS*

The VIMOS Ultra-Deep Survey (VUDS; Le Fèvre et al. 2015)[3] is a survey of $\sim$10 000 faint galaxies in the redshift range $2 < z \leq 6$ with i-band magnitudes down to $i \approx 27.0$ AB. The spectroscopic targets were also selected based on either reliable photometric redshifts or the presence of a Lyman break (LBGs) at higher redshifts, similar to VANDELS.

From the VUDS survey, we select sources in the GOODS-S/CDFS field with redshift reliability greater than 95 per cent, where the redshift reliability flags are determined in a similar manner to VANDELS. We refer the reader to Le Fèvre et al. (2015) and Tasca et al. (2017) for more information about source selection, data reduction, and redshift measurements. In total we select 20 sources with reliable spectroscopic redshifts from VUDS.

2.2.3 *VIMOS10*

The publicly available VLT/VIMOS spectroscopic survey in GOODS-S (Balestra et al. 2010; VIMOS10) contains spectra obtained using both the Low Resolution and Medium Resolution grisms for galaxies up to $z \sim 3.5$ with B and R magnitudes $\sim$24−25 AB. The spectroscopic targets were predominantly LBGs, similar to VANDELS and VUDS. We only use sources that have 'secure' redshifts, i.e. $>$ 99 per cent confidence of being correct owing to the relatively lower integration times of this survey, and find that 43 sources satisfied our selection criteria.

2.2.4 *MUSE-WIDE survey*

In addition to photo-z or LBG selected spectroscopic targets, we query reliable spectroscopic redshifts from the publicly available MUSE-WIDE survey in the GOODS-S/CDFS field,[4] which is a 'blind' integral-field unit (IFU) survey carried out without photometric preselection (Urrutia et al. 2019). The unique aspect of surveys enabled by MUSE[5] on the VLT is that no photometric pre-selection is required prior to obtaining a spectroscopic redshift. Therefore, spectroscopically confirmed sources are often blindly selected, owing to their emission lines alone and not necessarily their photometric redshifts or Lyman (or Balmer) breaks, which may bias the target selection. The MUSE-WIDE Survey is capable of obtaining spectroscopic redshifts for 98 per cent of photometrically selected galaxies brighter than 24.0 AB in *HST*/F775W. This blind galaxy sample is therefore highly complementary to the photo-z or LBG selection implemented by other data sets used in this study.

From this survey, we select sources with redshifts $3.11 < z < 3.53$ and reliable spectroscopic redshifts, i.e. a 'confidence' value of 2 or 3, corresponding to an expected error rate of $\lesssim 10$ per cent in the correct identification of emission and absorption features (Urrutia et al. 2019). We find that 44 galaxies in the MUSE-WIDE data release satisfy our selection criteria.

2.2.5 *MUSE-HUDF survey*

We also use the published spectroscopic redshifts from the MUSE deep (coverage area of 3×3 arcmin^2) and ultra deep (coverage area of 1×1 arcmin^2) surveys in the Hubble Ultra Deep Field (HUDF; Inami et al. 2017),[6] which is part of the GOODS-S field. This survey is deeper than MUSE-WIDE and is capable of blindly detecting sources as faint as $\approx$30.0 AB in *HST*/F775W (Inami et al. 2017).

We find that 42 sources from MUSE-HUDF lie in the redshift range of interest and have reliable spectroscopic redshifts, represented by confidence levels 2 and 3 and these sources are added to our sample.

2.2.6 *3D*-HST

Additional redshifts were queried from the 3D-*HST* survey, which is a spectroscopic survey conducted using the WFC3/G141 as well as the ACS/G800L grisms on the *HST* covering $\sim$600 arcmin^2 of well-studied extragalactic fields, including GOODS-S (Brammer et al. 2012; Momcheva et al. 2016). The 3D-*HST* survey obtained blind spectroscopy of galaxies, with the redshift determination primarily relying on the [O II] emission line in the redshift range of interest to this study. Since there was no photometric pre-selection required, the 3D-*HST* survey is similar to the MUSE surveys.

We add a further nine sources to our study from 3D-*HST* that have 'good' redshifts (`use_subj = 1`) from the the publicly available catalogues.[7]

[3] http://cesam.lam.fr/vuds/

[4] https://musewide.aip.de/project/

[5] https://www.eso.org/sci/facilities/develop/instruments/muse.html

[6] http://muse-vlt.eu/science/udf/

[7] https://3dhst.research.yale.edu/Data.php

Downloaded from https://academic.oup.com/mnras/article/511/1/120/6481640 by guest on 17 March 2023

Table 1. Number of sources with spectroscopic redshifts from data sets used in this study, at every stage of the selection described in Section 2.

Data set	*N*	Reference
Lyman-break (LBG) selected		
VANDELS DR4	90	(1, 2)
VUDS	20	(3, 4)
VIMOS10	43	(5)
Blind selected		
MUSE-WIDE	44	(6)
MUSE HUDF	42	(7)
3D-*HST*	9	(8)
Total	248	–
Total unique	**219**	–
Possible contaminants	34	–
Possible AGN	2	–
Final sample	**183**	–
Total LBG selected	111	–
Total blind selected	72	–

Note. References: (1) McLure et al. (2018); (2) Pentericci et al. (2018); (3) Le Fèvre et al. (2015); (4) Tasca et al. (2017); (5) Balestra et al. (2010); (6) Urrutia et al. (2019); (7) Inami et al. (2017); (8) Momcheva et al. (2016).

2.2.7 *Source duplication and final sample*

In total we shortlist 248 sources across the abovementioned surveys for this study, targeting galaxies based on photometric redshifts of Lyman-break selection, which we refer to as the Lyman break or LBG-selected, and those that were 'blindly' detected without any photometric pre-selection, which we refer to as the 'blind selected' sample. We note here again that although the spectroscopic surveys have different target selection strategies, we eventually require a detection in the PSF-homogenized CANDELS master photometric catalogue in GOODS-S for every source going forward.

Due to overlapping areas covered by the various spectroscopic surveys, a low fraction sources have been observed by multiple surveys. In such cases we give the highest precedence to the redshift obtained by VANDELS. In cases where the multiply detected source was not part of VANDELS, we give preference to the redshift recorded by the survey that is most sensitive out of the overlapping surveys.

Removing duplicate observations, 219 unique sources remain in our final sample and we show the breakdown of sources from various spectroscopic surveys in Table 1. We now turn our attention to filtering out sources that may suffer contamination to their LyC flux by emission from foreground sources along the line-of-sight using high-resolution *HST* photometry, as well as identifying possible AGN in the sample using deep X-ray data.

2.3 Identifying possible foreground contaminants

One of the biggest sources of error in the measurement of LyC signal from intermediate redshift galaxies is contamination within the aperture from emission from foreground galaxies along the line of sight to the source of interest (e.g. Vanzella et al. 2010). Therefore, before proceeding to measure LyC fluxes it is important to identify and remove sources that suffer from possible contamination to their LyC signal in the form of image artefacts, bright neighbouring sources or low-redshift interlopers along the line of sight. We adopt a series of steps, similar to Guaita et al. (2016), to filter the sample in order to maximize the accuracy of the LyC signal measurement.

Since all sources in our sample lie within the footprint of the GOODS-S field, they benefit from deep *HST* photometry at optical and near-infrared wavelengths from the *HST* Treasury Program (Dickinson et al. 2003) and through CANDELS (Grogin et al. 2011; Koekemoer et al. 2011), offering unparalleled resolution. This resolution is critical in the identification of possible foreground neighbouring sources in the vicinity of the galaxies with spectroscopic redshifts (e.g. Mostardi et al. 2015) that may strongly contaminate any LyC signal observed from the relatively lower resolution ground-based images.

To identify potential contamination, we create 20 × 20 arcsec^2 postage stamps from images in the F435W, F606W, F775W, and F850LP *HST* filters using publicly available images.[8] We also create postage stamps of the same dimensions in the LyC images. Sources that appear to be isolated in the *HST* images, without any other component or a nearby source within 1 arcsec of their centroid coordinates are shortlisted for LyC signal measurement without any further filtration. An example of such a source (with postage stamp sizes of 5 × 5 arcsec^2 for clarity) is shown in the top panel of Fig. 2.

For sources that have one or more components within a radius of 1 arcsec of the centroid in the *HST* images, we must determine whether these are a part of the galaxy in question (which may have a 'clumpy' morphology) or whether they are possibly foreground objects (e.g. Grazian et al. 2016). In the bottom panel of Fig. 2 we show an example (with 5 × 5 arcsec^2 postage stamps for clarity) where the spectroscopically confirmed source is surrounded by a nearby source that lies within 1 arcsec. Following Guaita et al. (2016), we examine the colours of the central galaxy and the surrounding components to identify contaminants in the following way. Using the F435W (*B*), F606W (*V*), F775W (*i*), and F850LP (*z*) images, we generate BGR colour images using the *make_lupton_rgb* function of *astropy.visualization* in *BVi*, *BVz*, *BIz*, and *VIz*. Additionally, we also produce a $V - z$ image for all sources. By then comparing the colours of the spectroscopically confirmed target and its companion(s) within 1 arcsec, we determine whether the component(s) close to the centroid of the source is (are) part of the system or not. For example, Fig. 3 shows the *Viz* colour image for the source shown in the bottom panel of Fig. 2, which is indicative that the companion source is likely to be a foreground contaminant.

Guaita et al. (2016) showed that the abovementioned simpler and more computationally efficient colour-based foreground identification method is highly effective at identifying interlopers. Such an analysis also returns a comparable contamination identification fraction compared to a full SED-fitting based analysis of the individual components surrounding the spectroscopically confirmed source. We also stress that removing sources that show clumps of different colours is a highly conservative approach, as it might result in the removal of galaxies with clumpy morphologies where the individual clumps may harbour slightly different stellar populations.

Through this process, we remove 34 sources from our initial sample of 220 unique sources, representing ≈ 15 per cent of the sample and bringing the sample size of unique sources that are unlikely to suffer from foreground contamination to 186. The fraction of sources removed due to possible contamination by foreground objects is highly consistent with an expected fraction of 12.6 per cent for $z \gtrsim 3$ galaxies determined by Vanzella et al. (2010), down to the photometric depths considered in this study assuming a 1 arcsec radius for contaminant identification.

[8] https://archive.stsci.edu/pub/hlsp/goods/v2/h_goods_v2.0_rdm.html

Downloaded from https://academic.oup.com/mnras/article/511/1/120/6481640 by guest on 17 March 2023

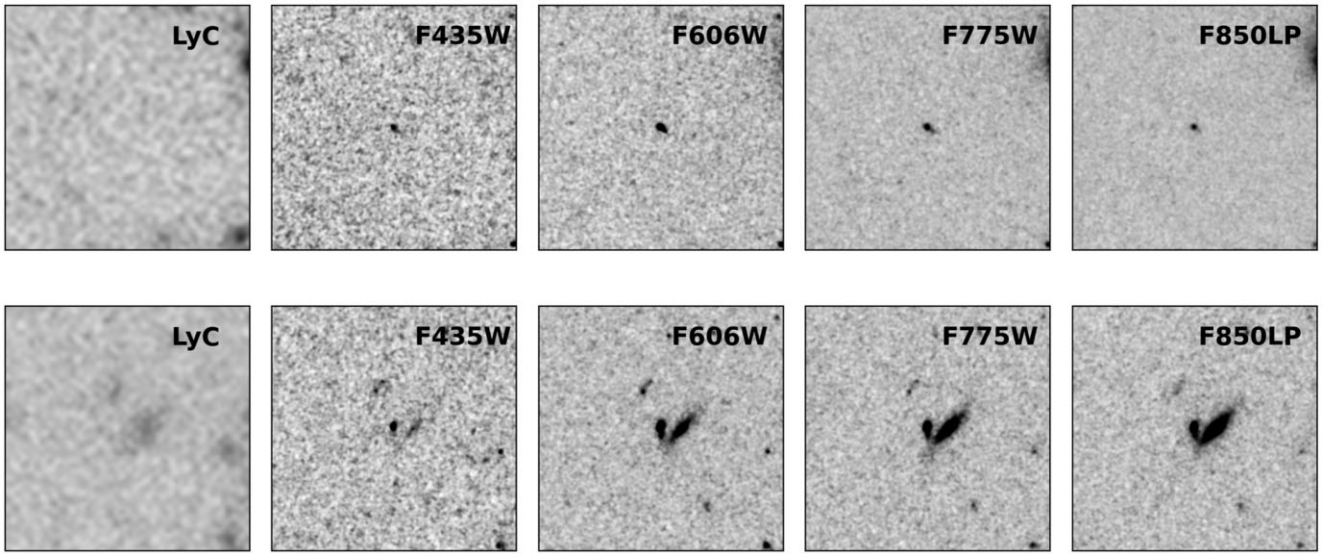


Figure 2. Ground-based LyC and *HST* postage stamps (5×5 arcsec^2) for a target galaxy that is isolated (top) and a target galaxy that has a possible foreground contaminant within 1 arcsec (bottom). For galaxies that are likely contaminated by foreground objects, examining the colours of both the target galaxy and the contaminant aids considerably in identifying photometric contamination in the LyC bands by a foreground galaxy (see Fig. 3) that is often mistakenly interpreted as LyC signal (e.g. Mostardi et al. 2015; Grazian et al. 2016; Guaita et al. 2016).

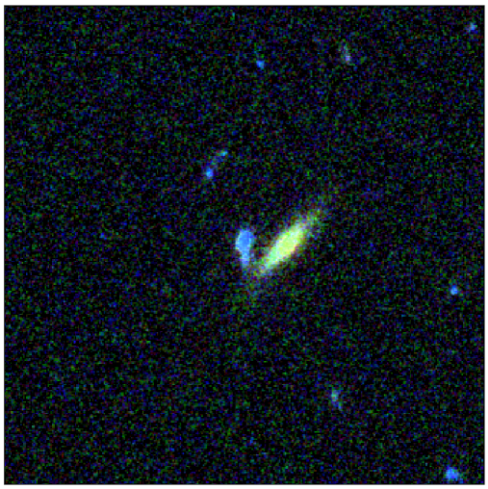


Figure 3. Colour image (5×5 arcsec^2) using the F606W (blue), F775W (green), and F850LP (red) *HST* filters of the central and companion galaxy of the example shown in the bottom panel of Fig. 2. The colour of the companion is clearly different from the central galaxy that is of interest, which indicates that the companion source is likely a foreground object.

2.4 Removing possible AGN

Finally, we remove potential AGN from our sample by cross-matching the coordinates of our sources with the *Chandra* 7 Ms source catalogue compiled by Luo et al. (2017) using a matching radius of 1.0 arcsec. The sources detected in the Luo et al. (2017) catalogue at $z \gtrsim 3$ are very likely to be AGN, owing to X-ray luminosities of $>10^{42}$ erg s^{-1} at these redshifts (e.g. Magliocchetti et al. 2020; Saxena et al. 2020a, 2021). We identify and remove two sources with counterparts in the X-ray catalogue that are also classified as AGN in the catalogue and therefore, the total number of sources in our final sample comes to 183.

2.5 Final sample

After removing duplicates, sources with foreground contamination and AGN from our sample, the total number of unique galaxies in the redshift range $3.11 < z < 3.53$ with reliable spectroscopic redshifts is 183.

The median spectroscopic redshift of our sample is $z = 3.38$ and our sample includes the known overdensity of star-forming galaxies at $z \sim 3.5$ in GOODS-S reported by Forrest et al. (2017). The median *HST*/F606W band magnitude of the galaxies in the final sample is 25.69 ± 0.84. We now proceed to fit SED models to the photometric data available to derive key galaxy physical parameters.

3 SED FITTING AND PHYSICAL PROPERTIES

Since the main aim of this study is to explore the dependence of LyC $f_{\rm esc}$ on key galaxy properties such as stellar masses, star-formation rates, etc. in addition to statistically exploring the correlations between $f_{\rm esc}$ and the strength of rest-frame nebular emission lines tracing intense star-formation such as [O III] + Hβ, obtaining robust and reliable SED fits using high quality photometry of galaxies in our sample is crucial.

These key galaxy properties are potentially important factors that govern $f_{\rm esc}$ from reionization era galaxies, and in this section we use deep *HST* and *Spitzer*/IRAC photometry in the observed frame optical and near-infrared bands, complemented by deep ground-based *K*-band photometry in combination with reliable spectroscopic redshifts to accurately constrain the stellar population properties and dust extinction for the 183 sources in our final sample. We additionally compare the derived physical properties of galaxies in our sample that were LBG selected, and those that were blind selected, exploring any inherent differences in galaxies that these two selection techniques may introduce, thereby impacting the inferred $f_{\rm esc}$.

3.1 SED-derived physical properties

To determine both the properties of stellar populations as well as the [O III] + Hβ line strengths using *K*-band photometry, we

Downloaded from https://academic.oup.com/mnras/article/511/1/120/6481640 by guest on 17 March 2023

simultaneously fit the stellar continuum and nebular line emission to the observed broad-band photometry of galaxies in our sample. We note that since both stellar continuum and nebular emission are being simultaneously fitted, we include the line-contaminated *K*-band photometry in the fitting.

The SED fitting is performed using the Bayesian Analysis of Galaxies for Physical Inference and Parameter EStimation (BAGPIPES) code (Carnall et al. 2018). BAGPIPES is a PYTHON based tool to generate complex galaxy model spectra, allowing flexible fitting to photometric data to derive key galaxy physical properties. As mentioned earlier, we use a combination of stellar continuum and nebular emission when fitting the SEDs. The stellar models are based on Bruzual & Charlot (2003), constructed using the Kroupa & Boily (2002) initial mass function (IMF). The nebular emission is computed using Cloudy grids (Ferland et al. 2013), with the only free parameter being the log of the ionization parameter (log U). When determining the strengths of the emission lines from these grids, the metallicity of the line-emitting gas is assumed to be the same as that of the stars.

We assume an exponentially declining star-formation history (τ-model), with stellar ages allowed to vary between 10 Myr and the age of the Universe at the observed redshift of the galaxy. The value of τ is allowed to vary between 100 Myr to 10 Gyr, with stellar metallicities allowed to vary in the range 0–1 $Z_{\odot}$, where $Z_{\odot}$ is the solar metallicity. The Calzetti et al. (2000) dust attenuation law is applied and the dust extinction, A_{1400} is allowed to vary between 0 and 2 mag. We use flat posterior distributions for each of the parameters, which is the default choice in BAGPIPES. The nebular emission line strengths are set by the log U parameter, which we allow to vary from -3 to -2, which are the typically inferred values for $z \gtrsim 3$ star-forming galaxies (see Nakajima et al. 2018; Saxena et al. 2020b, for example).

The chi-squared values of the best-fitting SEDs are evaluated, and individual SEDs are then visually inspected to ensure that the broad-band photometry, and crucially the *K*- band flux, are well reproduced by the best-fitting model. The best-fitting SEDs are then used to infer key physical properties for each galaxy, such as stellar age, dust attenuation, stellar mass, metallicity, star-formation rates, etc., in addition to the fluxes and rest-frame equivalent widths of the [O III] λ5007 and the H β lines derived from the nebular component of the best-fitting SED. Thanks to the Bayesian inference methodology of BAGPIPES, posterior distributions for all physical parameters are derived, leading to accurate uncertainty estimates.

The strength of the nebular emission that is added to the stellar continuum using BAGPIPES crucially depends on the best-fitting metallicity as well as the ionization parameter (see Carnall et al. 2018). Although the ionization parameter is a variable that can be controlled, the best-fitting metallicities are inferred from the broad-band SED fitting using both stellar and nebular components.

The median stellar mass (with 1σ standard deviation) derived from SED fitting of all 183 galaxies is $\log(M_{\star}/M_{\odot}) = 9.2 \pm 0.5$, the median star-formation rate is $8 \pm 24\,M_{\odot}\,yr^{-1}$, the median stellar age is 1.5 ± 1.4 Gyr, and the median stellar metallicity is $0.6 \pm 0.3\,Z_{\odot}$, where $Z_{\odot}$ is the solar metallicity (Asplund et al. 2009). Overall, the population of galaxies considered in this study are consistent with low-mass, star-formation objects with young stellar ages and low stellar metallicities.

In Fig. 4, we show the distribution of the derived stellar masses and star-formation rates of all the galaxies in the final sample. We mark the LBG-selected galaxies in our sample using blue points, and the emission line selected galaxies using orange squares. The histograms of both stellar masses and SFRs for the LBG and blind selected samples are also shown. We show the star-forming main sequence at $3 < z < 4$ determined by Santini et al. (2017) using dashed lines.

The majority of galaxies in our sample lie on or around the main sequence, and that the stellar masses and star-formation rates vary over a large range. We also find that as expected, the blind selected galaxies tend to occupy the lower stellar mass end of the main-sequence, consequently also exhibiting lower star-formation rates compared to LBG-selected galaxies.

We note here, however, that owing to the magnitude limited nature of our galaxy sample, a larger fraction of galaxies with lower stellar masses detected in the spectroscopic surveys will cluster towards higher SFRs, as is evident from Fig. 4, thereby resulting in an overall higher sSFR probed at lower stellar masses. Such an effect can potentially bias any possible dependence of LyC f_{esc} on key galaxy properties such as stellar mass and/or sSFR.

3.2 [O III] + H β line strengths

The best-fitting SED includes a stellar continuum and a nebular emission line component, from which the equivalent width of the emission lines can be calculated. Particularly for the [O III] and H β lines that fall in the observed *K* broad-band, we measure a median EW_0([O III] + H β) of $\approx$230 Å with standard deviation 225 Å, with the LBG selected sample having a median EW_0([O III] + H β) =236.2 Å and the blind selected sample having a slightly lower median EW_0([O III] + H β) = 207.2 Å. The distribution of EW_0([O III] + H β) measured for LBGs and blind selected galaxies is shown in Fig. 5.

The most immediate comparison for our [O III] + H β equivalent widths can be made with the study of Forrest et al. (2017), where using *K*-band photometry for galaxies at $2.95 < z < 3.65$ they report an average EW_0([O III] + H β) =230 $\pm$ 90 Å, which is highly comparable to the median value we find for our sample. In Fig. 6 we compare our SED derived line measurements with the best-fitting relations derived between spectroscopic measurements of the [O III] λ5007 line and the stellar masses of a large sample of star-forming galaxies at $z \sim 2$ as part of the MOSDEF survey (Reddy et al. 2018). We additionally show the stellar mass dependence of the [O III] line derived for a sample of extreme emission line galaxies (defined as EW_0([O III]) >225 Å by Tang et al. 2019) at $z \sim 2$ by Tang et al. (2019), which also exhibit lower stellar masses.

We find that the distribution of EW_0([O III]) as a function of stellar mass for galaxies in our sample broadly agrees with the best-fitting relation derived from MOSDEF at higher stellar masses. The scatter around the best-fitting relation observed in our sample is also consistent with what was reported by Reddy et al. (2018).

We identify 59 galaxies in our sample that can be classified as extreme emission line galaxies (EELGs), with EW_0([O III] + H β) >300 Å (e.g. Stark 2016)). The median EW_0([O III] + H β) in the EELG sample is $\approx$500 Å, which is slightly lower than the range of $\approx$660–800 Å reported by Forrest et al. (2017) for EELGs in their sample.

To further investigate the reliability of our inferred [O III] + H β line strengths, we compare our rest-frame [O III] + H β equivalent width measurements as a function of galaxy stellar to results from the MOSDEF spectroscopic survey (Kriek et al. 2015), which spectroscopically observed a sample of $\sim$1200 star-forming galaxies at redshifts $1.4 \lesssim z \lesssim 3.8$ (Reddy et al. 2018) in Fig. 6. We find that our measurements at $z \sim 3$–3.5 broadly agree with the best-fitting relation obtained by Reddy et al. (2018), with comparable scatter at stellar masses $>10^9\,M_{\odot}$.

Downloaded from https://academic.oup.com/mnras/article/511/1/120/6481640 by guest on 17 March 2023

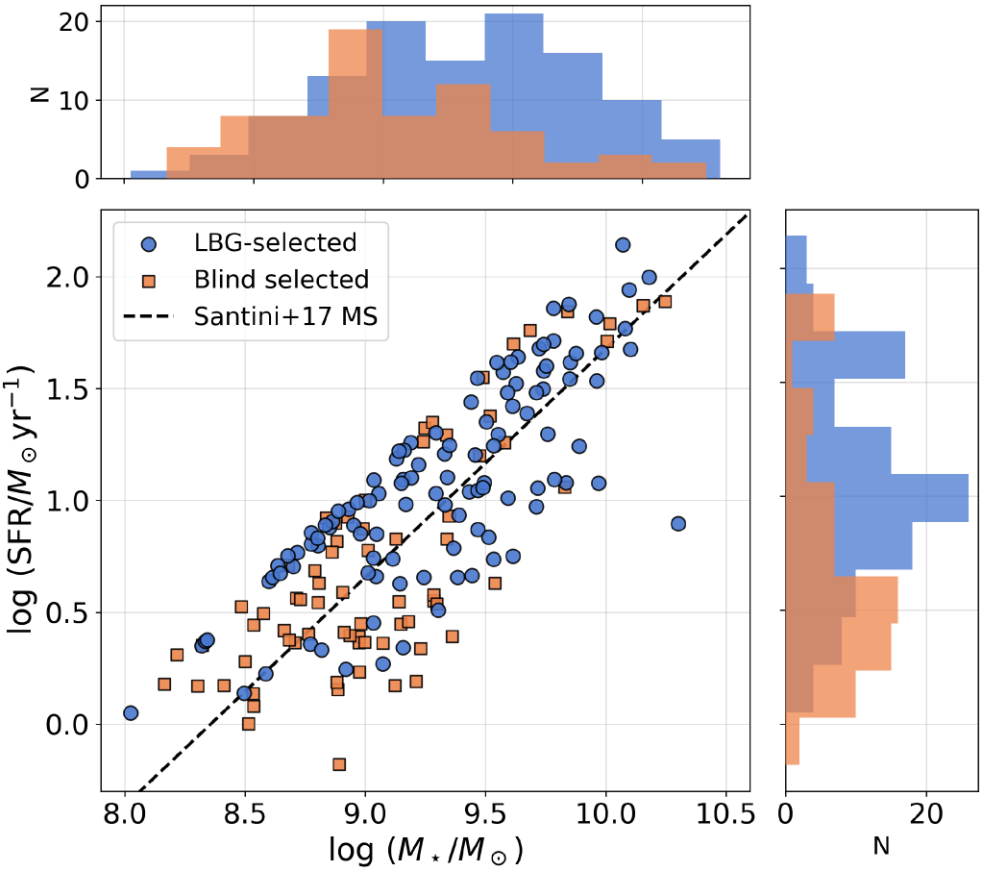


Figure 4. Distribution of SED-derived stellar masses and star-formation rates for galaxies in the final sample, colour coded by metallicity. The dashed line shows the star-forming main sequence derived by Santini et al. (2017) at redshifts $3 < z < 4$. We find that most of our galaxies lie on the main sequence, and span a range of masses and star-formation rates, which makes them representative of the general galaxy population at $z \sim 3.3$.

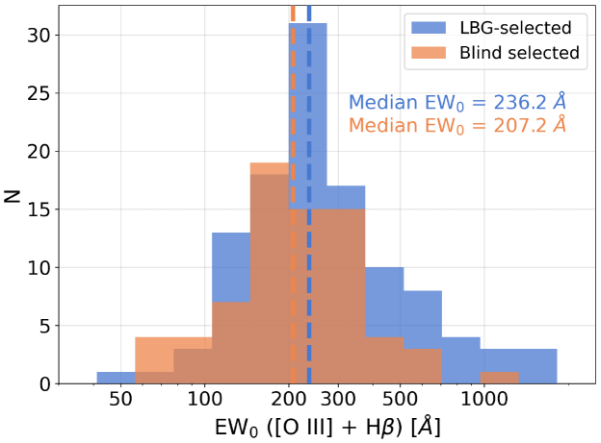


Figure 5. Histogram of the rest-frame [O III] + Hβ equivalent widths measured for LBG-selected galaxies (blue) and blind selected galaxies (orange) in our sample using SED fitting. The median EW$_0$([O III] + Hβ) of the full sample is 228.6 Å, and the derived equivalent widths follow a lognormal distribution (similar to that reported by Stark et al. 2013). The EW distributions for both LBGs and emission line galaxies are comparable, with the median values (dashed lines and text) highly consistent with each other.

We also compare EWs of galaxies in our sample that may be considered as EELGs following the Tang et al. (2019) classification (EW$_0$([O III]) >225 Å) with spectroscopic measurements at $z \sim 2$ from Tang et al. (2019), finding broad agreement with their best-fitting relation (Tang et al., private communication), which is also shown in Fig. 6.

Our EELG [O III] + Hβ EWs are also comparable with photometrically selected extreme line emitters found at $z > 6$ – Endsley et al. (2021) measured a median value of EW$_0$([O III] + Hβ) ∼700 Å for star-forming galaxies at $z \sim 7$ and Labbé et al. (2013) found an average rest frame [O III] + Hβ EW of 670 ± 200 Å at $z \sim 8$. Additionally, Smit et al. (2015) identified galaxies with extreme *Spitzer*/IRAC colours at $z \sim 6.8$ and found that 50 per cent of the strongest line emitters have EW$_0$([O III] + Hβ) ∼1085 Å. Using a similar technique, Roberts-Borsani et al. (2016) identified four bright galaxies at $z \sim 7$ with EW$_0$([O III] + Hβ) ∼1500 Å, all of which have been confirmed to be strong Lyα emitters. Further, Castellano et al. (2017) measured an average EW([O III] + Hβ) of ∼1500 Å for Lyα emitting galaxies at $z \sim 6.8$. Therefore, our sample of EELGs at $z \sim 3$–3.5 offers an excellent opportunity to study the escaping ionizing radiation from analogues of reionization-era galaxies.

We note here, however, that the line strengths of some of the brightest [O III] + Hβ emitting galaxies, particularly those with fainter continua, may be underestimated due to the lower limit on the

Downloaded from https://academic.oup.com/mnras/article/511/1/120/6481640 by guest on 17 March 2023

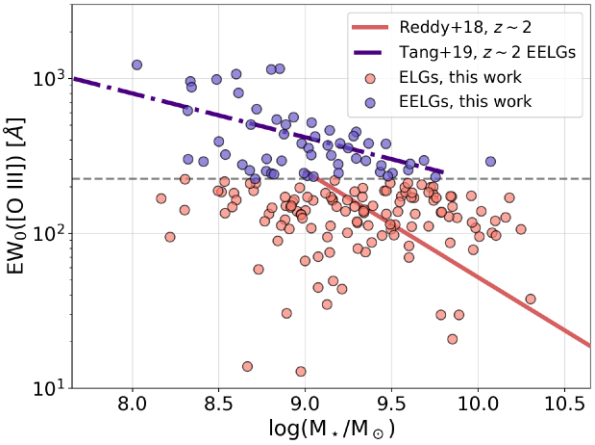


Figure 6. Distribution of EW_0([O III]) and galaxy stellar mass derived for our sample of galaxies using SED fitting. Shown for comparison are the best-fitting relations derived between the two quantities for relatively massive star-forming galaxies at $z \sim 2$ by Reddy et al. (2018) (red solid line) from the MOSDEF survey and extreme emission line galaxies (EELGs) at $z \sim 2$ by Tang et al. (2019) (blue dot-dashed line), where the black dashed line marks EW_0([O III]) >225 Å, used by Tang et al. (2019) to classify galaxies as EELGs. The normalization of the best-fitting relations have not been altered. Galaxies from our sample that would be considered as normal emission line galaxies (ELGs) are shown as red points, and those considered as EELGs are shown using blue points. The distribution of our SED derived measurements (and the scatter) are broadly consistent with spectroscopic measurements at lower redshifts.

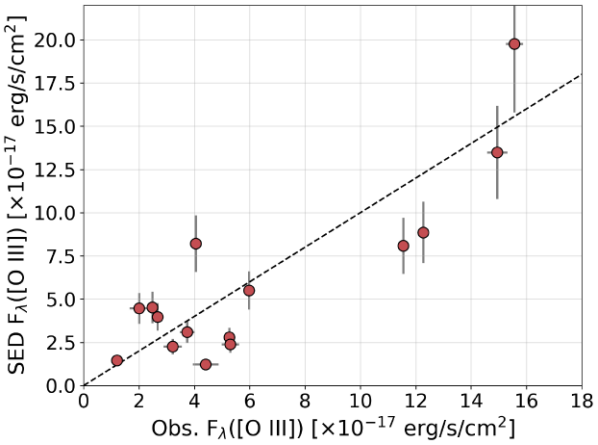


Figure 7. Comparison of [O III] + H β line fluxes measured from the best-fitting SED and *K*-band excess and the observed line fluxes from NIR spectra. From the limited number of galaxies in our sample that have observed line fluxes from Cullen et al. (2021), we can conclude that our method of estimating line fluxes from *K*-band excess works reasonably well.

ionization parameter of −2.0 permitted by BAGPIPES as well as the depth of photometric data in the *K* band. We further note that the flux (and consequently stellar mass) limited nature of our galaxy sample naturally results in incompleteness of EELGs down to lower stellar masses.

3.3 Comparison with NIR spectroscopic observations

To test the accuracy of the inferred [O III] + H β strengths from SED fitting, we compare our measurements with near-IR observations of a subset of VANDELS galaxies in the CDFS and UDS fields in the redshift range $z \sim 3$–4 using MOSFIRE on Keck Telescope, as part of the recently completed NIRVANDELS survey (Cullen et al. 2021). We note that only a fraction of NIRVANDELS galaxies in the CDFS field are also part of the final sample in this study.

To do this, we fit SEDs to all NIRVANDELS galaxies using the same SED fitting parameters and techniques that we used for the main galaxy sample described in Section 3 and compare the observed and SED-derived [O III] line fluxes. The comparison between the SED derived and observed [O III] line fluxes for NIRVANDELS galaxies is shown in Fig. 7, with the dashed line marking the one-to-one relation. The error bars shown on the SED derived line fluxes are at the 20 per cent level. We find that the SED derived line fluxes are remarkably close to the observed values (within ∼0.3 dex) over a broad flux range. We therefore conclude that simultaneously fitting the stellar continuum and nebular line emission with the ionization parameter in the range $-3 \leq \log U \leq -2$ gives realistic estimates of the [O III] (and H β) line fluxes for galaxies in our sample.

Having fitted SEDs to all 183 unique galaxies in our final sample and measured key galaxy properties as well as [O III] and H β line strengths, we now proceed to measure LyC fluxes for galaxies using the available LyC images.

4 LYMAN CONTINUUM ESCAPE FRACTION

4.1 Measuring $f_{\rm esc}^{\rm rel}$ and $f_{\rm esc}$

In this section we describe our methodology for measuring the LyC flux from the available LyC images. Since these filters cover slightly different rest-frame LyC wavelengths at different redshifts as mentioned in Section 2.1, we split our sample into the relevant redshift bins corresponding to LyC coverage offered by the filters. *NB3727* includes 79 galaxies, *NB396* includes 83 galaxies, and *U* includes 91 galaxies. We show the number of galaxies and the redshift ranges corresponding to each LyC filters along with 1σ depths in Table 2. We note that owing to the overlapping wavelength coverage offered by the *NB396* and the *U*-band filter, some galaxies are included in both subsets.

An important parameter quantifying the escape of LyC photons from a galaxy in a dust-independent manner is the relative $f_{\rm esc}$, or $f_{\rm esc}^{\rm rel}$ (Steidel, Pettini & Adelberger 2001), comparing the observed ratio of ionizing to non-ionizing UV flux to the intrinsically produced ratio by stellar populations within the galaxy, corrected for absorption by the intervening neutral IGM. If the intrinsic ratio of luminosities at ∼1400 Å and ∼900 Å, $(L_{1400}/L_{900})_{\rm int}$ is known (e.g. from stellar population modelling), then $f_{\rm esc}^{\rm rel}$ can be calculated as

$$f_{\rm esc}^{\rm rel} = \left(\frac{F_{900}}{F_{1400}}\right)_{\rm obs} \times \left(\frac{L_{1400}}{L_{900}}\right)_{\rm int} \times \frac{1}{\exp\left(-\tau_{900}\right)}, \quad (1)$$

where $(F_{900}/F_{1400})_{\rm obs}$ is the observed ratio of the ionizing LyC flux to non-ionizing UV flux at ∼1400 Å, and $\tau_{900}^{\rm IGM}$ is the transmissivity of ionizing photons (at 900 Å) through the intervening IGM (Siana et al. 2007). The absolute escape fraction, $f_{\rm esc}$, can then be calculated from $f_{\rm esc}^{\rm rel}$ by applying a dust correction as follows

$$f_{\rm esc} = f_{\rm esc}^{\rm rel} \times 10^{(-0.4 \times A_{1400})}, \quad (2)$$

where $A_{1400} = 10.33 \times E(B-V)$ according to the Calzetti et al. (2000) dust reddening law. Therefore, to calculate $f_{\rm esc}$ we must constrain each of these ingredients in equations (1) and (2), and below we highlight how these are calculated for our galaxies.

Downloaded from https://academic.oup.com/mnras/article/511/1/120/6481640 by guest on 17 March 2023

Table 2. LyC filters used in this study along with 1σ depths (see Section 2.1), LyC redshift range covered and the number of sources. Note that some sources have overlapping LyC coverage in *NB396* and *U* images.

Filter	Tel./Instr.	1σ depth (AB)	z range	N	Reference
NB3727	CTIO 4m/MOSAICII	27.38	3.11–3.34	79	Guaita et al. (2016)
NB396	La Silla 2.2m/WFI	27.72	3.41–3.53	83	Guaita et al. (2016)
U band	VLT/VIMOS	29.78	3.34–3.49	91	Nonino et al. (2009)

4.1.1 *LyC flux measurement*

The observed flux ratios in the equations above require a measurement of the LyC flux, which we measure from the available LyC images using aperture photometry. Photometry in the LyC images is performed by placing circular apertures at the coordinates in the CANDELS catalogues using the PYTHON package PHOTUTILS (Bradley et al. 2020). The average PSF of the *NB3727* image is 1.4 arcsec, of the *NB396* is 0.94 arcsec (Guaita et al. 2016) and of the *U* image is 0.8 arcsec (Nonino et al. 2009). The radius of the circular aperture is set to either match or be slightly larger than the PSF to capture small-scale PSF variations across the LyC images. Therefore, we use an aperture with radius 0.7 arcsec for *NB3727* and 0.5 arcsec for *NB396* and *U*-band images.

We measure the local background noise around the apertures by placing a circular annulus (at the same positions as the aperture) with an inner radius of 2 arcsec and an outer radius of 3 arcsec. For galaxies in which the flux measured in the aperture was lower than the background flux measured in the annulus, we assigned a limiting LyC flux value equal to the local background noise with a 100 per cent error.

The non-ionizing UV flux is calculated from the F606W *HST* image, which covers the rest-frame ∼1400 Å wavelengths for the redshift range of galaxies in this study. Therefore, the ratio of the flux determined from the LyC bands and from the F606W band gives us a measure of the term $(F_{900}/F_{1400})_{\rm obs}$.

4.1.2 *Intrinsic non-ionizing to ionizing luminosity ratio*

The intrinsic ratio between UV luminosity at non-ionizing wavelengths (e.g. ∼1400 Å) and LyC wavelengths (∼900 Å) is calculated individually for each source using the best-fitting SED. We create synthetic SEDs using the best-fitting stellar population parameters determined and measure the intrinsic ratios, L_{1400}/L_{900}, for each galaxy.

We find an average intrinsic ratio of 4.5, with a standard deviation of 0.7. Individual intrinsic ratio measurements for each galaxy enabled by accurate spectroscopic redshifts lead to a more accurate $f_{\rm esc}$ calculation for individual galaxies compared assuming an average intrinsic ratio for all galaxies in the sample, as done by previous studies measuring LyC $f_{\rm esc}$ at $z \sim 3$, where the assumed intrinsic ratio took values of 3 (Steidel et al. 2001; Grazian et al. 2016, 2017; Marchi et al. 2017), 5 (Guaita et al. 2016; Vanzella et al. 2016a), or 7 (Fletcher et al. 2019).

4.1.3 *IGM transmissivity*

We calculate the IGM transmissivity of LyC photons for each galaxy using the prescriptions of Steidel et al. (2018). In addition to the IGM transmission, the Steidel et al. (2018) model also takes into account the effects of transmission through the circumgalactic medium (CGM) surrounding each galaxy in the so-called 'IGM + CGM' model. This results in an average LyC transmission, $\exp(-\tau_{900}) = 0.371$ at $z = 3.0$ and a much lower $\exp(-\tau_{900}) = 0.264$ at $z = 3.5$.

An advantage of having spectroscopic redshifts is that the IGM transmission can be accurately calculated for each source at the rest-frame wavelength of 900 Å, the τ_{900}. Hence, we calculate the LyC transmission through both the IGM and the CGM, or $\exp(-\tau_{900})$ for each galaxy in our final sample.

4.1.4 *Dust attenuation*

Finally, the dust attenuation (or A_{1400}) for each source is calculated from the best-fitting SED. During the SED fitting process we allowed A_{1400} to vary between 0 and 2, which naturally limits the derived values. This means that our SED fits will miss any significantly dusty galaxies, but given the high-redshift star-forming nature of these galaxies, heavy dust obscuration is unlikely to be the case. We find an average dust attenuation of $A_{1400} = 0.40$ mag in our sample with a standard deviation of 0.26 mag.

Having defined the necessary ingredients to calculate $f_{\rm esc}$ for each source and described the measurements of each of these parameters, in the following section we present the measurements of the relative and the absolute escape fractions of LyC photons from each galaxy.

4.2 Individual LyC $f_{\rm esc}$ measurements

We measure non-zero LyC $f_{\rm esc}$ at $\gtrsim 2\sigma$ significance levels in 11 out of 183 galaxies in our sample. The LyC $f_{\rm esc}$ is in the range of 0.14–0.85, and the galaxies showing non-zero $f_{\rm esc}$ span a wide range of stellar masses ($M_\star = 10^{8.3}$–$10^{9.7}$ M$_\odot$), star-formation rates (SFR = 2.3–37.4 M$_\odot$ yr^{-1}), and [O III] + Hβ equivalent widths (EW$_0$([O III] + Hβ) =111.8–1160.3 Å).

We note that 8 out of 11 candidate LyC leakers were LBG selected, and 3 were blindly selected for spectroscopic follow-up. The galaxy with the highest measured $f_{\rm esc}$ =0.85 ± 0.33 (CDFS 13385) was blindly selected from the MUSE-HUDF survey and has a relatively low stellar mass of $10^{8.3}$ M$_\odot$, showing extreme [O III] + Hβ line emission through its *K*-band photometry.

The best-fitting SED derived physical parameters for these 11 candidate LyC leaking galaxies are given in Table 3, and the measured quantities (both through SED fitting and aperture photometry) used to calculate $f_{\rm esc}^{\rm rel}$ and $f_{\rm esc}$ are given in Table 4. The 5 × 5 arcsec^2 cutout galleries showing the LyC image and the observed-frame optical *HST* photometry, along with the best-fitting SEDs for the 11 LyC leaker candidates are shown in Fig. A1 in Appendix A. A full spectroscopic analysis of these 11 LyC leaking candidates is beyond the scope of this paper and will be explored in greater detail in forthcoming publications.

It is important to note that given the stochasticity of the IGM attenuation at these redshifts (see for example Bassett et al. 2021), it is hard to accurately determine the absolute LyC $f_{\rm esc}$ for sources at $z \gtrsim 3$. Therefore, the IGM stochasticity introduces an unavoidable element of scatter in the $f_{\rm esc}$ measurements, which in turn may be an important source of scatter in the correlations between $f_{\rm esc}$ and key

Downloaded from https://academic.oup.com/mnras/article/511/1/120/6481640 by guest on 17 March 2023

Table 3. Nature of selection for each galaxy, with LBG representing Lyman-break selected and BLD representing blind selection, as well as best-fitting SED-derived physical properties for candidate LyC leaking galaxies. Also given is the LyC detection filter for each source.

CANDELS ID	Sample	Survey	z	LyC filter	$\log(M_\star/M_\odot)$	SFR ($M_\odot$ yr^{-1})	log(sSFR/yr^{-1})	EW$_0$ ([O III] + Hβ) (Å)
CDFS 5161	LBG	VANDELS	3.420	NB396	9.3	16.3	−8.1	268.2
CDFS 9358	LBG	VIMOS10	3.229	NB3727	9.6	37.0	−8.1	241.3
CDFS 9692	LBG	VANDELS	3.470	NB396	8.3	2.3	−8.0	1160.3
CDFS 12448	LBG	VANDELS	3.460	U	9.6	12.5	−8.5	119.3
CDFS 13385	BLD	MUSE HUDF	3.431	U	8.6	3.6	−8.1	334.6
CDFS 15718	BLD	MUSE HUDF	3.439	NB396	8.3	2.0	−8.0	986.8
CDFS 16444	BLD	MUSE HUDF	3.128	NB3727	9.3	23.1	−7.9	456.4
CDFS 18454	LBG	VUDS	3.163	NB3727	9.2	16.7	−8.0	339.8
CDFS 19872	LBG	VANDELS	3.452	NB396	9.6	5.6	−8.8	111.8
CDFS 20745	LBG	VANDELS	3.495	NB396	9.0	5.5	−8.3	400.6
CDFS 24975	LBG	VANDELS	3.187	NB3727	9.7	19.8	−8.5	214.9

Table 4. Parameters required for the calculation of $f_{\rm esc}^{\rm rel}$ and $f_{\rm esc}$ for candidate LyC leakers identified in this study.

CANDELS ID	z	$(L_{1400}/L_{900})_{\rm int}$	A_V (mag)	F_{900} (μJy)	$(F_{900}/F_{1400})_{\rm obs}$	$<\exp(-\tau_{900})>$	$f_{\rm esc}^{\rm rel}$	$f_{\rm esc}$
CDFS 5161	3.420	3.7	0.6 ± 0.1	0.036 ± 0.015	0.07 ± 0.02	0.28	0.91 ± 0.39	0.53 ± 0.24
CDFS 9358	3.229	3.4	0.5 ± 0.1	0.048 ± 0.020	0.02 ± 0.01	0.32	0.21 ± 0.11	0.14 ± 0.07
CDFS 9692	3.470	2.3	0.4 ± 0.1	0.039 ± 0.020	0.06 ± 0.03	0.27	0.55 ± 0.25	0.38 ± 0.19
CDFS 12448	3.460	4.1	0.1 ± 0.1	0.006 ± 0.001	0.02 ± 0.01	0.27	0.24 ± 0.10	0.20 ± 0.12
CDFS 13385	3.431	3.5	0.3 ± 0.1	0.009 ± 0.002	0.09 ± 0.02	0.28	1.12 ± 0.24	0.85 ± 0.33
CDFS 15718	3.439	2.0	0.4 ± 0.1	0.034 ± 0.009	0.06 ± 0.02	0.28	0.42 ± 0.12	0.28 ± 0.10
CDFS 16444	3.128	3.0	0.7 ± 0.1	0.068 ± 0.014	0.06 ± 0.01	0.34	0.55 ± 0.11	0.30 ± 0.07
CDFS 18454	3.163	2.2	0.8 ± 0.1	0.045 ± 0.021	0.04 ± 0.02	0.34	0.42 ± 0.21	0.20 ± 0.10
CDFS 19872	3.452	4.0	0.1 ± 0.1	0.040 ± 0.020	0.02 ± 0.01	0.28	0.32 ± 0.16	0.29 ± 0.30
CDFS 20745	3.495	4.0	0.2 ± 0.1	0.033 ± 0.015	0.03 ± 0.02	0.27	0.45 ± 0.23	0.38 ± 0.30
CDFS 24975	3.187	3.4	0.7 ± 0.1	0.043 ± 0.021	0.05 ± 0.02	0.33	0.53 ± 0.21	0.27 ± 0.11

galaxy properties that will be investigated in the sections that follow. We will discuss the effects of IGM stochasticity on the inferred LyC $f_{\rm esc}$ measurements in Section 6.

Given the relatively large sample size of 183 sources, we expect ≈4 sources to appear as noise fluctuations at the 2σ level. From Table 4 we note that 4 out of 11 sources identified as candidate LyC leakers are close to the 2σ confidence level in their respective LyC images and could be consistent with noise fluctuations. Deeper photometric data at LyC wavelengths is needed to confirm the LyC leaking nature of these sources.

Apart from the 11 candidate LyC leakers, all other galaxies in our sample remain undetected at $\gtrsim 2\sigma$ levels in the available LyC images, indicating that the global $f_{\rm esc}$ from star-forming galaxies at $z = 3$–3.5 must be low. In the sections that follow we derive the global $f_{\rm esc}$ from different populations of galaxies in our sample through stacking the low-significance LyC fluxes measured from the majority of galaxies, and use these stacked measurements to set additional constraints on any global dependence of $f_{\rm esc}$ on key galaxy properties traced by subpopulations of galaxies within our sample.

4.3 Stacked LyC $f_{\rm esc}$ measurements

Only ≈ 6 per cent galaxies in our sample have a $\gtrsim 2\sigma$ detection in the LyC images. Therefore, to constrain the global $f_{\rm esc}$ we must co-add the LyC signal from galaxies that were not classified as candidate LyC leakers. To do this, we first remove the 11 individual LyC leakers from the stacking sample and employ both the stacking of LyC images, as well as co-adding the LyC flux measured through aperture photometry as described below.

We first investigate whether any LyC signal can be measured through stacking the LyC images of individual galaxies falling within the redshift coverage of each LyC filter. To do this, we produce 10 × 10 arcsec^2 cutouts of both the LyC image and the corresponding root-mean-squared (RMS) error image centred on the CANDELS coordinates for galaxies that are not individual LyC leakers. We then apply 5σ clipping to the cutouts to masks bright pixels that could bias the stacked image. We then co-add the sigma-clipped cutouts using a weighted averaging method, where the corresponding RMS of each pixel of the galaxy cutout is used to assign a weight to the pixels of each galaxy cutout. In Fig. 8 we show the results from stacking the LyC cutouts for each of the filters and as can be seen, we do not find any statistically significant LyC signal even in the stacked *NB3727*, *NB396*, and *U*-band images, consistent with that reported by Guaita et al. (2016) from the two narrow bands and by Naidu et al. (2018) from the *U* broad-band.

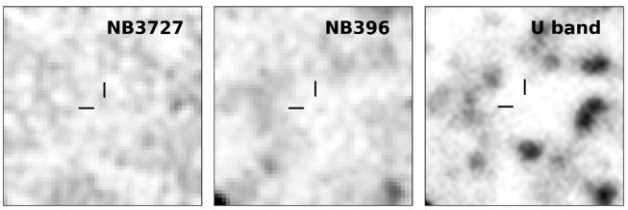


Figure 8. Stacked image from all sources in *NB3727* (left-hand panel), *NB396* (middle), and *U* band (right-hand panel). We do not see any statistically significant flux in any of the stacked images.

Instead of extracting a flux from these stacked LyC images and relying on the sample averaged values for the intrinsic non-ionizing to ionizing UV ratio, IGM transmissivity and dust attenuation to calculate $f_{\rm esc}$, we use a slightly different approach and derive global $f_{\rm esc}$ using the standard deviation of the weighted average of the

Downloaded from https://academic.oup.com/mnras/article/511/1/120/6481640 by guest on 17 March 2023

Table 5. Physical properties and f_{esc} for LBG or blind selected galaxies, ELGs and EELGs, and the full sample. Note that the LBG and blind selected subsets are created only for those galaxies that are undetected in the LyC images at $\gtrsim 2\sigma$ level, but the ELG and EELG subsets include the individual LyC leakers as well.

Subset	N	$\log(M_\star/M_\odot)$	$\log(\mathrm{sSFR/yr}^{-1})$	EW_0 ([O III] + H β) (Å)	f_{esc}
LBG selected, LyC non-detections	103	9.4	−8.2	236.2	<0.11
Blind selected, LyC non-detections	69	9.0	−8.3	207.2	<0.13
ELGs (all) – EW_0([O III] + H β) <300 Å	124	9.3	−8.3	183.5	<0.14
EELGs (all) – EW_0([O III] + H β) ≥300 Å	59	8.9	−8.0	421.2	<0.20
Full sample	183	9.2	−8.3	230.9	<0.16

individual LyC fluxes measured through aperture photometry across the available LyC images as described in Section 4.1.1 (see also Guaita et al. 2016). The weight assigned to the f_{esc} measurement for each source is the inverse square of the error on f_{esc}, or $1/\Delta f_{esc}^2$.

After background subtraction, the weighted average of sources that are not classified as candidate LyC leakers would be expected to be close to zero, with the standard deviation providing a robust 1σ upper limit on the LyC signal from the sample (see also Guaita et al. 2016). This method takes full advantage of the availability of spectroscopic redshifts and accurate SED fitting that enable reliable measurements of both the values, errors, and limits on individual f_{esc}^{rel} and f_{esc} for each galaxy.

Galaxies in the redshift range covered by *NB3727* do not overlap with the other two LyC filters. However, galaxies with redshifts between 3.41 and 3.49 have overlapping LyC coverage in both *NB396* and *U* images. Therefore, to assign a LyC flux and f_{esc} to each unique galaxy in our sample, we prioritize the flux measured from the LyC image with a lower error, which translates to a lower error on f_{esc}. We note here that f_{esc} measurements/limits recorded using both LyC filters are broadly in agreement with each other.

Using the standard deviation of the weighted average of LyC flux from the unique sample of galaxies that are not individually identified as LyC leakers, we obtain a 1σ upper limit of f_{esc} <0.12. We additionally calculate the stacked f_{esc} limit obtained from all galaxies in the sample (i.e. both LyC detections and non-detections) finding a slightly higher 1σ limit of f_{esc} <0.16, which is not surprising. This stacked measurement from the full sample potentially helps minimize the effects of stochastic IGM transmission along the line of sight, which we discuss further in Section 6.

4.3.1 *LyC* f_{esc} *from LBG and blind selected galaxies*

Out of the 172 galaxies that were not identified as individual LyC detections, 103 are LBG selected and 69 are blindly selected. Using weighted averaging, we derive 1σ f_{esc} limits of <0.11 for the LBG selected and a slightly higher 1σ limit of <0.13 for the blind selected sample. We note here that since the blind selected sample is also fainter in UV magnitudes, the flux limited nature of the available LyC images may bias the inferred f_{esc} to higher values.

A LyC f_{esc} <0.11 for our LBG selected sample is comparable with $f_{esc} \approx 0.09$ reported by Steidel et al. (2018) by stacking deep UV spectra of $z \sim 3$ LBGs and $f_{esc} \approx 0.06$ obtained by a later reanalysis of the Steidel et al. (2018) sample by Pahl et al. (2021), and with other measurements from LBGs at $z \sim 3$ (e.g. Grazian et al. 2016; Guaita et al. 2016; Marchi et al. 2017; Naidu et al. 2018; Meštrić et al. 2021). The slightly higher 1σ f_{esc} limit of f_{esc} <0.13 measured for blind-selected galaxies is also consistent with measurements of emission-line selected galaxies at $z = 2$–4 (e.g. Mostardi et al. 2015; Japelj et al. 2017; Ji et al. 2020; Smith et al. 2020).

4.3.2 *LyC* f_{esc} *from extreme emission line galaxies (EELGs)*

In this section we investigate the stacked f_{esc} measurements of the previously identified EELGs (EW_0([O III] + H β) ≥300 Å) as well as normal emission line galaxies (ELGs; EW_0([O III] + H β) <300 Å) in our sample (see Section 3.2). For this analysis we include the 11 candidate LyC leakers to better understand the dependence of f_{esc} on [O III] + H β EWs.

There are 59 EELGs and 124 ELGs in our sample. The average EW_0([O III] + H β) for EELGs is 421.2 Å and the average EW_0([O III] + H β) for ELGs is 183.5 Å. By once again calculating the weighted average of f_{esc} for ELGs and EELGs, we determine 1σ upper limits of f_{esc} <0.14 for ELGs and f_{esc} <0.20 for EELGs. We note here that we obtain slightly higher f_{esc} limits from bins created based on emission line strengths compared to the LBG and blind-selected samples because the individually identified LyC leakers are included in the ELG and EELG bins.

Qualitatively speaking, the distribution of [O III] + H β EWs measured for individual LyC leakers is similar to the distribution of the parent sample, implying that the individual LyC leakers seem to have been randomly drawn from the parent sample at least in terms of [O III] + H β EWs. This is consistent with what was reported by Nakajima et al. (2020) for a sample of LAEs at $z \sim 3$, where the [O III] + H β EWs of LAEs that are LyC leakers and non-leakers are not significantly different.

In Table 5 we give the median galaxy physical properties and the measured f_{esc} for subsets created based on the initial spectroscopic selection method, as well as on the strength of [O III] + H β emission lines. No clear differences in f_{esc} are seen between these subsets, posing questions surrounding the origin of leaking LyC radiation from only a low fraction of galaxies at intermediate redshifts. In the following section we investigate the dependence of f_{esc} on key galaxy properties for both candidate LyC leakers and stacks of galaxies.

5 RESULTS

Having measured LyC fluxes and f_{esc} values for every source in the sample, and having used stacking to establish f_{esc} limits from the sample of galaxies that do not show any LyC leakage, in this section we explore potential correlations between f_{esc} and the properties of the underlying stellar population in the galaxies. Constraining the dependence of f_{esc} on these key galaxy properties is important to understand the key drivers of reionization at $z > 6$, and here we rely on robust SED-fitting based measurements to explore these.

5.1 Dependence of f_{esc} on stellar mass

We first explore the dependence of f_{esc} on the stellar masses of galaxies. In Fig. 9 we show the f_{esc} measured for the candidate LyC leaking candidates as well as the stacked limits obtained for the subsamples of LBG and blind selected galaxies in our sample. As

Downloaded from https://academic.oup.com/mnras/article/511/1/120/6481640 by guest on 17 March 2023

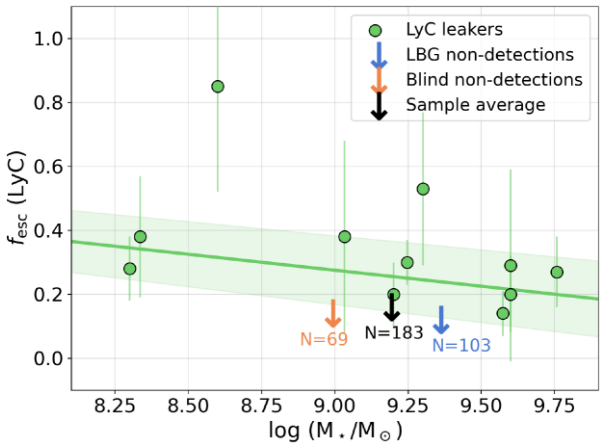


Figure 9. LyC f_{esc} as a function of stellar mass for candidate LyC leakers in our sample (green points), and stacked measurements from LBG selected (blue arrow), blind-selected galaxies (orange arrow) and the sample average (black arrow) in this study. The number of galaxies used in the stacking measurement are also given. We find a very weak correlation between f_{esc} and stellar mass, with a best-fitting slope -0.10 ± 0.02 (solid green line, uncertainty in shaded region). This dependence on stellar mass is stronger than the recently observed lack of correlation between the two quantities for a sample of low mass ($< 10^8\ M_\star$) galaxies at $0.3 \lesssim z \lesssim 0.45$ by Izotov et al. (2021), however the scatter is very large. We note that the stacked limits are not included when obtaining the best-fitting relations in this study.

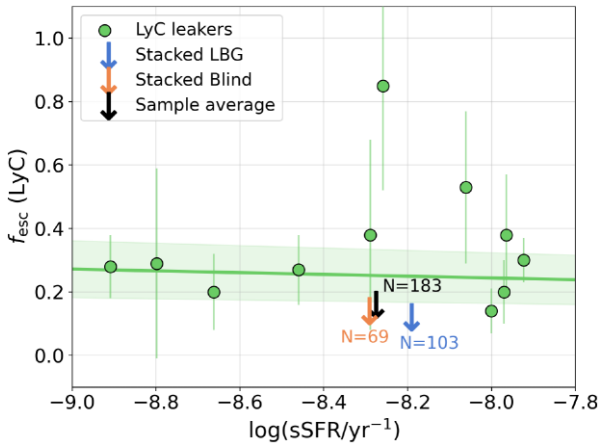


Figure 10. Distribution of f_{esc} and sSFR of candidate LyC leakers, LBG, and blind-selected galaxies as well as the sample average (same legend as Fig. 9). We find little to no correlation between f_{esc} and sSFR of individual LyC leakers at the 2σ confidence level, with a best-fitting slope -0.028 ± 0.015 (solid green line with uncertainty in shaded region). The stacked f_{esc} values derived from LBG and blind-selected samples are consistent with the best-fitting relation. The lack of dependence of f_{esc} on sSFR has also been seen in simulations (e.g. Yoo et al. 2020).

reported in Section 3.1, the median stellar mass of LBG selected galaxies is $10^{9.3}$ M$_\odot$ and that of the blind selected galaxies is $10^{9.0}$ M$_\odot$.

We find that the candidate LyC leaking galaxies occupy a large range of stellar masses, ranging from $10^{8.3} - 10^{9.7}$ M$_\odot$. The galaxy with the highest f_{esc} in our sample, CDFS 13385 at $z = 3.431$ with $f_{esc} = 0.85 \pm 0.33$ has a stellar mass of $\approx 10^{8.3}$ M$_\odot$, which is lower than the stellar masses of known LyC leaking galaxies with $f_{esc} > 0.5$ at $z \gtrsim 3$ such as *Ion2* (de Barros et al. 2016; Vanzella et al. 2016a), *Ion3* (Vanzella et al. 2018) and Q1549−C25 (Shapley et al. 2016), and comparable to the stellar masses of LyC leaking LAEs identified by Fletcher et al. (2019). The LyC leaker with the highest stellar masses in our sample has $M_\star \approx 10^{9.7}$ – CDFS 24975 at $z = 3.187$ with $f_{esc} = 0.27 \pm 0.11$.

We use least-squares fitting to obtain the best-fitting parameters for the function $f_{esc} = A \log(M_\star/\mathrm{M}_\odot) + B$, finding $A = -0.10 \pm 0.02$ and $B = 1.17 \pm 0.40$ (solid green line in Fig. 9). The slope of the best-fitting relation suggests a very weak dependence of f_{esc} on the stellar mass of galaxies in our sample. Although not very strong, the mass dependence of f_{esc} that we report from our candidate LyC leakers is stronger than the no apparent mass dependence reported by Izotov et al. (2021) for a sample of very low mass ($M_\star < 10^8$ M$_\odot$) galaxies in the redshift range $z = 0.31-0.45$.

We also find that there is no clear difference in the upper limits of f_{esc} obtained by stacking samples of LBG-selected and blind-selected galaxies. Blind-selected galaxies on average have lower stellar masses, and a slightly higher f_{esc} upper limit, which is consistent with the mass dependence obtained by fitting measurements for the candidate LyC leakers in our sample.

5.2 Dependence of f_{esc} on specific SFR

We now investigate correlations between f_{esc} and specific SFR (sSFR), which is the star-formation rate per unit stellar mass of a galaxy. The distribution of f_{esc} and sSFR for both the candidate LyC leakers and stacks of LBG and blind selected galaxies is shown in Fig. 10. As reported in Section 3.1, the blind selected galaxies in our sample have a slightly lower median specific SFR of $\log(\mathrm{sSFR/yr^{-1}}) = -8.3$ compared to $\log(\mathrm{sSFR/yr^{-1}}) = -8.2$ for LBG selected galaxies.

The candidate LyC leakers cover a large range of sSFRs, from $\log(\mathrm{sSFR/yr^{-1}}) \approx -8.8$ to $\log(\mathrm{sSFR/yr^{-1}}) \approx -7.9$. We note that the majority of LyC leaking candidates (seven out of 11) have relatively high sSFR values, with $\log(\mathrm{sSFR/yr^{-1}}) \gtrsim -8.1$, comparable to LyC leaking LAEs from Fletcher et al. (2019). In particular, the strongest LyC leaker in our sample, CDFS 13385, has $\log(\mathrm{sSFR/yr^{-1}}) = -8.1$, which is lower than *Ion2* and *Ion3* but more than an order of magnitude higher than Q1549−C25 (Shapley et al. 2016).

To quantify the dependence of f_{esc} on sSFR, we again use least-squares fitting and obtain best-fitting correlations to the function $f_{esc} = C \log(\mathrm{sSFR/yr^{-1}}) + \mathrm{D}$ with a slope of $C = -0.028 \pm 0.015$ (solid green line in Fig. 10). This best-fitting suggests a very weak decrease of f_{esc} with increasing sSFR, but is consistent with no dependence of f_{esc} on sSFR at the $\approx 2\sigma$ confidence level, consistent with what has been reported from disc galaxy simulations at high redshifts (e.g. Yoo, Kimm & Rosdahl 2020).

Assuming that the stellar mass of a galaxy is closely linked to its size at UV wavelengths, no strong dependence of f_{esc} on sSFR may also translate to no strong dependence of f_{esc} on the star-formation surface density of galaxies (e.g. Model II of Naidu et al. 2020). This may have bearing on the dominant contribution of the UV brightest sources towards reionization, and accurate size measurements of our candidates LyC leakers that will be explored in a future study will help robustly test the dependence of f_{esc} on SFR surface densities.

5.3 Dependence of f_{esc} on [O III] + H β strengths

In this section, we investigate the dependence of f_{esc} on the [O III] + H β line strengths for galaxies in our sample. In Fig. 11 we show the f_{esc} and the log of $\mathrm{EW_0}$([O III] + H β) for individual LyC leakers (green points) as well as limits derived for normal

Downloaded from https://academic.oup.com/mnras/article/511/1/120/6481640 by guest on 17 March 2023

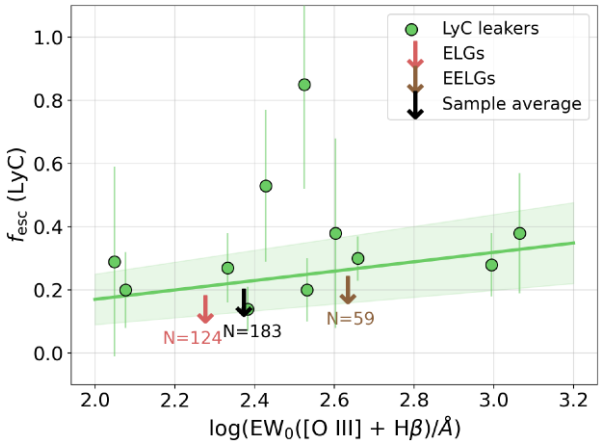


Figure 11. Distribution of f_{esc} and log(EW$_0$([O III] + H β)/Å) for individual sources (green points) and limits derived for ELGs (red arrow) and EELGs (brown arrow) in our sample. We find a positive correlation between f_{esc} and the strength of the [O III] + H β lines for the candidate LyC leaker candidates, with best-fitting slope of 0.15 ± 0.04. High [O III] + H β line fluxes are seen when the physical conditions within a galaxy favour low metallicities or intense star-formation activity, which are important conditions to both produce a large number of LyC photons as well as facilitate a high escape fraction of these photons.

ELGs (red arrow) and EELGs (brown arrow), which were defined in Section 4.3.2. We note that 6 out of the 11 individual LyC leakers can be classified as EELGs, with EW$_0$([O III] + H β) >300 Å.

For the individual LyC leaking candidates, CDFS 9692 at z = 3.470 with f_{esc} =0.38 ± 0.19 has the highest EW$_0$([O III] + H β) value of 1160.3 Å. The strongest LyC leaker, CDFS 13385, also shows extreme [O III] + H β line fluxes, with EW$_0$([O III] + H β) = 986.8 Å, in line with expectations from galaxies with high f_{esc}. However, overall we do not find consistently high [O III] + H β EWs across our candidate LyC leaking galaxies. Similarly, as reported in Section 4.3.2 we do not find a considerably higher f_{esc} using stacking for EELGs compared to the sample of ELGs, but do find that the f_{esc} limit for EELGs is higher than that for ELGs.

A best-fitting relation between f_{esc} and [O III] + H β line strengths shows a positive correlation, indicating that galaxies with higher f_{esc} also tend to show stronger [O III] + H β lines, shown in Fig. 11. The best-fitting relation has a positive slope of 0.15 ± 0.04, indicative of a mild dependence of f_{esc} on rest-frame [O III] + H β EW, with the general trend of increasing f_{esc} at higher [O III] + H β strengths consistent with what has been seen in the local Universe (e.g. Izotov et al. 2018a). The higher f_{esc} upper limit of <0.20 seen for EELGs compared to f_{esc} <0.14 seem for ELGs is also consistent with the best-fitting relation obtained.

NIR spectroscopy of LyC leaking LAEs from the Fletcher et al. (2019) sample presented by Nakajima et al. (2020), however, did not find uniformly high [O III] + H β line strengths for LyC leakers, which is consistent with our findings. Izotov et al. (2018a) reported a large spread in the f_{esc} values of local LyC leaking galaxies with high [O III] line strengths. Therefore, there is increasing evidence that suggests that high [O III] + H β line strengths may be a necessary condition for f_{esc}, but are by no means sufficient to guarantee high f_{esc}. This is reflected in our galaxy sample as well, where galaxies with extremely high [O III] + H β strengths do not all necessarily appear to be strong LyC leakers.

We also note here that given the volume limited nature of the spectroscopic galaxy survey data used in this study, and the rarity on the sky of extreme line emitting galaxies, we are likely to miss several extreme [O III] + H β line emitters in our sample. Studies investigating correlations between f_{esc} and strength of [O III] + H β emission (or [O III]/[O II] ratios) have largely focused on galaxy samples at relatively low redshifts, and the lack of completeness of extreme line emitters that are likely to exhibit high f_{esc} is a caveat of any attempt to investigate the dependence of f_{esc} on [O III] + H β strength at $z > 3$ from our data set.

Therefore, our analysis has found a weak negative correlation between f_{esc} and stellar mass, but contrary to expectations of models of reionization, we do not see any significant correlation between f_{esc} and specific SFR of galaxies. We have also found that only a small fraction (≈ 6 per cent) of galaxies in our sample can be reliably classified as candidate LyC leakers, although the uncertainties on the measured f_{esc} are large owing to low significance of the measured LyC flux. The question that naturally arises following these findings, and is paramount to understanding the nature of sources in the early Universe that drove the bulk of reionization, is: What regulates f_{esc} in a galaxy? We discuss the relevance and implications of our findings in the following section.

6 DISCUSSION – WHAT REGULATES f_{ESC}?

The escape fraction of ionizing photons from star-forming galaxies crucially depends on the fraction of ionizing radiation absorbed/scattered by the neutral gas and dust around the photon emitting regions. To have high f_{esc}, a large amount of neutral gas and dust must have been expelled from the star-forming regions through either supernova or AGN feedback (e.g. Wise et al. 2014; Trebitsch et al. 2017, 2018; Barrow et al. 2020; Katz et al. 2020). Given the dependence of high f_{esc} from star-forming galaxies on the presence of ionized channels through which LyC photons can escape into the IGM, the orientation of the galaxies and potential (mis)alignment of these channels with the observer will play a key role in whether or not a galaxy appears to be leaking LyC radiation (e.g. Borthakur et al. 2014).

Therefore, by selection only a fraction of intermediate redshifts reionization era analogue galaxies in any given sample will be identified as LyC leakers, assuming that these galaxies uniformly leak non-zero fractions of LyC photons. This geometrical misalignment of the viewing angles of a majority of sources may explain the relatively low numbers of individual galaxies identified in our sample, and across other samples that appear to be leaking significant fractions of LyC photons (e.g. Fletcher et al. 2019). A further explanation to the relatively low f_{esc} values seen in the more relatively massive star-forming galaxies at intermediate redshifts could be the higher metallicities compared to the ultralow metallicities expected from galaxies in the reionization era (Yoo et al. 2020).

Another important factor that has an impact on whether or not a galaxy selected from a large sample appears to be a LyC leaker is the stochasticity of the IGM along the line-of-sight. Using ensembles of simulated IGM transmission functions along multiple lines-of-sight at $z \gtrsim 3$, Bassett et al. (2021) showed that for a given underlying distribution of LyC f_{esc} in a galaxy sample, only those galaxies that lie along sightlines with higher IGM transmission appear to be leaking LyC radiation, exhibiting high f_{esc}. Inclusion of a possible IGM transmission bias for both candidate LyC leakers and non-leakers in this work may result in reduced f_{esc} values for the leakers, with an increase in the upper limits of f_{esc} inferred from stacking the non-leakers (e.g. Bassett et al. 2021).

In addition to observational effects such as orientation or stochastic IGM transmission, theoretical modelling has also revealed complex

Downloaded from https://academic.oup.com/mnras/article/511/1/120/6481640 by guest on 17 March 2023

relationships between stellar population properties such as metallicity, ionization parameter, etc. and f_{esc}, which impact the observed f_{esc} and its dependence on physical properties of stars in a star-forming galaxy (e.g. Bassett et al. 2019). Further complexities are introduced by geometrical and viewing angle effects that further impact correlations between f_{esc} and the strength of the ionizing radiation field and ionizing photon production rates from young stars traced by strong [O III] + H β line strengths (e.g. Katz et al. 2020), among other galaxy properties. Barrow et al. (2020) showed that the periods during which a galaxy exhibits intense star-formation activity and ionizing photon production, and periods corresponding to high f_{esc} may be non-coincident, with high periods of f_{esc} often following starburst activity (see also Kimm & Cen 2014; Trebitsch et al. 2017; Kakiichi & Gronke 2021).

However, it is important to note that conditions enabling high f_{esc} following a starburst event may not necessarily coincide with an equally high production rate or efficiency of ionizing photons (ξ_{ion}), as also seen in the simulations of Barrow et al. (2020). Therefore, there is an element of fortuitousness introduced in whether or not a star-forming galaxy selected from a large sample at any given epoch appears to be leaking LyC photons, and crucially depends on periods of both high ξ_{ion} as well as high f_{esc} being coincident (see also Fletcher et al. 2019; Nakajima et al. 2020).

Further, a spatially resolved analysis of the lensed LyC leaker dubbed 'Sunburst' at $z = 2.37$ (Dahle et al. 2016; Rivera-Thorsen et al. 2019) recently showed that a young massive star cluster dominates the leaking LyC radiation from the entire galaxy ($f_{esc}^{rel} \approx 0.43$–$0.93$), whereas older clusters show considerably lower LyC f_{esc} values (Vanzella et al. 2021). Without magnification due to lensing, the spatially unresolved Sunburst arc would exhibit a much lower LyC leakage overall ($f_{esc}^{rel} \approx 0.06-0.12$) as the LyC radiation escaping along other lines of sight would be missed due to insufficient LyC imaging depths (see also Vanzella et al. 2020).

Therefore, in a scenario where a large fraction of LyC photons produced by only a limited number of individual young star clusters within galaxies manage to escape into the IGM through favourably aligned channels, there would be increased scatter in the observed dependence of f_{esc} and galaxy properties such as stellar mass or specific SFR for any given sample of galaxies. Although this would explain the lack of significant correlations observed between f_{esc} and the physical properties of candidate LyC leakers in this study, most importantly with the sSFR, such an effect complicates the observational understanding of what regulates the escape of ionizing photons and consequently, which sources were the key drivers of reionization. This makes studying indicators that trace the presence of LyC photons escape channels and their dependence on key galaxy properties crucial to understanding the physical and geometrical conditions that enable a high apparent f_{esc} in the epoch of reionization (e.g. Steidel et al. 2018).

One such probe is the Ly α line, whose shape, width, and intensity can offer insights into LyC and Ly α escape channels from clusters of young stars within high redshift galaxies (e.g. Verhamme et al. 2017; Izotov et al. 2018a, b; Matthee et al. 2018; Vanzella et al. 2018, 2020; Meyer et al. 2021; Naidu et al. 2021). Additional high ionization emission lines like He II λ1640, C IV $\lambda\lambda$1548, 1550, and C III] $\lambda\lambda$1907, 1909 in the rest-UV may help trace stellar populations that produce copious amounts of ionizing photons, possibly leading to higher f_{esc} (e.g. Schaerer et al. 2018; Berg et al. 2019; Senchyna et al. 2019; Llerena et al. 2021). Saxena et al. (2020b) investigated He II emitting star-forming galaxies in the redshift range $z \sim 2.5$–5 and did not find any strong dependence of the presence or the strength of He II emission on the stellar mass or star-formation rates of galaxies (see also Nanayakkara et al. 2019), which may be consistent with factors that lead to a lack of observed dependence of f_{esc} on these properties as discussed above.

A key advantage of our galaxy sample at $z \approx 3$–3.5 is the availability of rest-frame UV spectra from various spectroscopic surveys, crucially also covering the Ly α emission line, and in a future study we will explore the correlations between f_{esc}, Ly α, and other rest-UV spectroscopic indicators for these newly discovered candidate LyC leakers (and non-leakers). *JWST* will give access, for the first time, to the full suite of rest-frame optical emission lines in $z > 3$ galaxies, enabling direct measurements of the ionizing radiation field strengths produced by young stars (through [O III] line strengths and [O III]/[O II] ratios) as well as measurements of the ionizing photon production efficiencies using H α measurements, which will considerably aid in identifying physical conditions within star-forming galaxies that lend themselves to high f_{esc}. The correlations between f_{esc} and rest-frame optical emission established at these intermediate redshifts will be instrumental in interpreting the ionizing photon escape of galaxies at $z = 6-9$, for which *JWST* will enable rest-optical spectroscopy, in a bid to understand the nature of the main drivers of reionization.

Therefore, going forward it is essential to obtain deeper LyC imaging for intermediate redshift analogues of reionization era galaxies to properly account for the viewing angle and orientation effects when measuring f_{esc}. Further, detailed studies of the rest-frame UV and optical spectra of known LyC leakers are needed to investigate the presence of LyC escape channels and study the dependence of these features on galaxy properties. Better insights into the time-scales and the incidence of high f_{esc} within star-forming galaxies may be needed from high-resolution simulations (e.g. Mauerhofer et al. 2021) of a larger number of reionization era galaxies (with sufficient time resolution) to temporally tie periods of intense star-formation to f_{esc} and other galaxy properties.

7 SUMMARY AND CONCLUSIONS

We have measured the Lyman continuum (LyC) escape fraction (f_{esc}) using ground-based LyC images available for 183 spectroscopically confirmed galaxies in the CDFS/GOODS-S field in the redshift range $3.11 < z < 3.53$. The spectroscopic redshifts are taken from publicly available data bases, that primarily targeted the higher mass Lyman break (LBG) selected galaxies or blindly discovered lower mass galaxies thanks to emission line surveys.

We use available deep *HST* photometry and colours at non-ionizing UV wavelengths to remove possible foreground contaminants that may strongly bias the inferred LyC flux and f_{esc} as well as accurately constrain the SEDs of our galaxies giving robust measurements of key galaxy properties. Using a combination of stellar and nebular emission, we also derive rest-frame optical emission line strengths, primarily the [O III] and H β line fluxes (that fall in the observed *K* band) for our galaxies.

We then measure LyC flux and f_{esc} using aperture photometry and detect LyC flux at $\geq 2\sigma$ significance levels in 11 out of 183 galaxies, with f_{esc} values ranging from 0.14−0.85. Around 94 per cent of the galaxies in our sample remain undetected at the $\gtrsim \sigma$ level, and using weighted averaging of their LyC f_{esc} limits, we place a 1σ upper limit of $f_{esc} < 0.12$ from the galaxies with no significant detections in the available LyC images. We additionally compare the weighted average f_{esc} limits from subsamples of galaxies that were LBG or blind-selected, finding 1σ limits of $f_{esc} < 0.11$ for LBG-selected and $f_{esc} < 0.13$ for blind-selected galaxies. We further place f_{esc} limits from normal ELGs; ([O III] + H β <300 Å) and EELGs

Downloaded from https://academic.oup.com/mnras/article/511/1/120/6481640 by guest on 17 March 2023

([O III] + Hβ >300 Å), finding 1σ limits of f_{esc} <0.14 for normal and f_{esc} <0.20 for extreme emission line galaxies.

Although the uncertainties on the measured f_{esc} values for the 11 candidate LyC leaking galaxies are high and a handful of sources have low signal-to-noise ratios in the LyC images ($\approx 2\sigma$), we find a weak negative correlation between f_{esc} and stellar mass at the 2σ level, with a shallow slope of -0.10 ± 0.02. We do not find any significant correlation between f_{esc} and specific star-formation rate of the individual LyC leakers at the 2σ level, with a slope of -0.028 ± 0.015. Lastly, we find a positive correlation between f_{esc} and EW$_0$([O III] + Hβ) for the candidate LyC leakers in our sample, suggesting that the [O III] + Hβ line strengths may be important indicators of f_{esc} as has been previously reported in the literature.

From our results, it remains unclear what the dominant galaxy property is when it comes to regulating f_{esc} in LyC leaking galaxies. The low detection fraction of LyC leakers across our sample is consistent with a scenario where LyC photons escape through discrete ionized channels within star-forming galaxies, which are seldom oriented along the line-of-sight of the observer. The time-dependent nature of high f_{esc} that often follows periods of intense star-formation also suggests that only a low fraction of galaxies at any given epoch would be actively leaking LyC photons, consistent with our observations.

The stochasticity of the intervening neutral intergalactic medium, which may play an important role in absorbing leaking LyC photons along the line-of-sight is another factor that may impact LyC detections. Future work tying LyC escape to the presence of ionized channels within galaxies using observations, exploration of the time-dependent nature of LyC leakage from larger samples of simulated reionization era galaxies as well as investigation of IGM stochasticity across redshifts are needed to fully understand these effects in the context of contribution of star-forming galaxies towards the cosmic reionization photon budget.

In conclusion, our work has discovered a sample of 11 previously undiscovered candidate LyC leakers at $z \sim 3$–3.5 adding crucial statistics that are needed to understand the escape of ionizing photons from intermediate redshift analogues of $z > 6$ galaxies. Studying lower redshift analogues of reionization era galaxies, where direct detection of escaping LyC radiation is possible, remains the only way to constrain LyC escape from star-forming galaxies that are expected to drive the bulk of reionization. An increased sample of LyC leaking galaxies complemented by deeper LyC/UV imaging, higher resolution spectra across wavelengths, and zoom-in simulations will help understand the unique physical conditions that drive high f_{esc}, bringing us a step closer towards unravelling the nature of galaxies and their ionizing radiation that drove cosmic reionization.

ACKNOWLEDGEMENTS

We thank the referee for constructive feedback that improved the quality of this work. AS thanks Ross McLure and Mario Nonino for useful input and discussions, Fergus Cullen for sharing NIR-VANDELS measurements and Mengtao Tang for sharing the best-fitting relation for emission line strengths from their analysis. AS and LP thank Alice Shapley for useful comments and discussions that improved the analysis presented.

AS and RSE acknowledge financial support from European Research Council Advanced Grant FP7/669253. DS and ASL acknowledge support from Swiss National Science Foundation. RA acknowledges support from ANID FONDECYT Regular 1202007. MLl acknowledges support from the National Agency for Research and Development (ANID)/Scholarship Program/Doctorado Nacional/2019-21191036.

This work makes use of VANDELS data. The VANDELS collaboration acknowledges the invaluable role played by ESO staff for successfully carrying out the survey. This work is based on VUDS data, obtained with the European Southern Observatory Very Large Telescope, Paranal, Chile, under Large Program 185.A-0791, and made available by the VUDS team at the CESAM data center, Laboratoire d'Astrophysique de Marseille, France. This work is based on observations taken by the MUSE-Wide and MUSE-HUDF Surveys as part of the MUSE Consortium. This work is based on observations taken by the 3D-*HST* Treasury Program (GO 12177 and 12328) with the NASA/ESA *HST*, which is operated by the Association of Universities for Research in Astronomy, Inc., under NASA contract NAS5-26555. MLl acknowledges support from the National Agency for Research and Development (ANID)/Scholarship Program/Doctorado Nacional/2019-21191036.

This work has made extensive use of JUPYTER and IPYTHON (Pérez & Granger 2007) notebooks, ASTROPY (Astropy Collaboration 2013, 2018), MATPLOTLIB (Hunter 2007), SEABORN (Waskom & the seaborn development team 2020), PANDAS (pandas development team 2020), and TOPCAT (Taylor 2005). This work would not have been possible without the countless hours put in by members of the open-source developing community all around the world, with special thanks to the Stackoverflow community.

DATA AVAILABILITY

The VANDELS data can be accessed using the VANDELS data base at http://vandels.inaf.it/dr4.html, or through the ESO archives. The VUDS data can be accessed from the VUDS webpage: http://cesam.lam.fr/vuds/ or ESO archives. MUSE data can be accessed from https://musewide.aip.de/project/ and http://muse-vlt.eu/science/udf/ and the 3D-*HST* data can be accessed from https://archive.stsci.edu/prepds/3d-hst/. The VIMOS10 data are available from Balestra et al. (2010). All the code used to perform the analysis in this paper was written in PYTHON and will be shared upon reasonable request to the corresponding author.

REFERENCES

Asplund M., Grevesse N., Sauval A. J., Scott P., 2009, ARA&A, 47, 481
Astropy Collaboration 2013, A&A, 558, A33
Astropy Collaboration 2018, AJ, 156, 123
Balestra I. et al., 2010, A&A, 512, A12
Barrow K. S. S., Robertson B. E., Ellis R. S., Nakajima K., Saxena A., Stark D. P., Tang M., 2020, ApJ, 902, L39
Bassett R. et al., 2019, MNRAS, 483, 5223
Bassett R., Ryan-Weber E. V., Cooke J., Meštrić U., Kakiichi K., Prichard L., Rafelski M., 2021, MNRAS, 502, 108
Berg D. A., Chisholm J., Erb D. K., Pogge R., Henry A., Olivier G. M., 2019, ApJ, 878, L3
Bian F., Fan X., 2020, MNRAS, 493, L65
Bian F., Fan X., McGreer I., Cai Z., Jiang L., 2017, ApJ, 837, L12
Borthakur S., Heckman T. M., Leitherer C., Overzier R. A., 2014, Science, 346, 216
Bradley L. et al., 2020, astropy/photutils: 1.0.0. Available at: https://doi.org/10.5281/zenodo.4044744
Brammer G. B. et al., 2012, ApJS, 200, 13
Bromm V., Yoshida N., 2011, ARA&A, 49, 373
Bruzual G., Charlot S., 2003, MNRAS, 344, 1000
Calzetti D., Armus L., Bohlin R. C., Kinney A. L., Koornneef J., Storchi-Bergmann T., 2000, ApJ, 533, 682

Downloaded from https://academic.oup.com/mnras/article/511/1/120/6481640 by guest on 17 March 2023

Carnall A. C., McLure R. J., Dunlop J. S., Davé R., 2018, MNRAS, 480, 4379
Castellano M. et al., 2017, ApJ, 839, 73
Cristiani S., Serrano L. M., Fontanot F., Vanzella E., Monaco P., 2016, MNRAS, 462, 2478
Cullen F. et al., 2021, MNRAS, 505, 903
Dahle H. et al., 2016, A&A, 590, L4
Dayal P., Ferrara A., 2018, Phys. Rep., 780, 1
Dayal P. et al., 2020, MNRAS, 495, 3065
de Barros S. et al., 2016, A&A, 585, A51
Dickinson M., Giavalisco M., GOODS Team, 2003, in Bender R., Renzini A., eds, The Mass of Galaxies at Low and High Redshift. Springer, Berlin , p. 324
Endsley R., Stark D. P., Chevallard J., Charlot S., 2021, MNRAS, 500, 5229
Faisst A. L., 2016, ApJ, 829, 99
Ferland G. J. et al., 2013, Rev. Mex. Astron. Astrofis., 49, 137
Finkelstein S. L. et al., 2019, ApJ, 879, 36
Fletcher T. J., Tang M., Robertson B. E., Nakajima K., Ellis R. S., Stark D. P., Inoue A., 2019, ApJ, 878, 87
Fontanot F., Cristiani S., Vanzella E., 2012, MNRAS, 425, 1413
Forrest B. et al., 2017, ApJ, 838, L12
Garilli B., Paioro L., Scodeggio M., Franzetti P., Fumana M., Guzzo L., 2012, PASP, 124, 1232
Garilli B. et al., 2021, A&A, 647, A150
Giallongo E. et al., 2015, A&A, 578, A83
Grazian A. et al., 2016, A&A, 585, A48
Grazian A. et al., 2017, A&A, 602, A18
Grazian A. et al., 2018, A&A, 613, A44
Grogin N. A. et al., 2011, ApJS, 197, 35
Guaita L. et al., 2016, A&A, 587, A133
Hunter J. D., 2007, Comput. Sci. Eng., 9, 90
Inami H. et al., 2017, A&A, 608, A2
Inoue A. K., Shimizu I., Iwata I., Tanaka M., 2014, MNRAS, 442, 1805
Izotov Y. I., Thuan T. X., Guseva N. G., 2017, MNRAS, 471, 548
Izotov Y. I., Schaerer D., Worseck G., Guseva N. G., Thuan T. X., Verhamme A., Orlitová I., Fricke K. J., 2018a, MNRAS, 474, 4514
Izotov Y. I., Worseck G., Schaerer D., Guseva N. G., Thuan T. X., Fricke, Verhamme A., Orlitová I., 2018b, MNRAS, 478, 4851
Izotov Y. I., Worseck G., Schaerer D., Guseva N. G., Chisholm J., Thuan T. X., Fricke K. J., Verhamme A., 2021, MNRAS, 503, 1734
Japelj J. et al., 2017, MNRAS, 468, 389
Jaskot A. E., Oey M. S., 2013, ApJ, 766, 91
Jaskot A. E., Dowd T., Oey M. S., Scarlata C., McKinney J., 2019, ApJ, 885, 96
Ji Z. et al., 2020, ApJ, 888, 109
Kakiichi K., Gronke M., 2021, ApJ, 908, 30
Katz H. et al., 2020, MNRAS, 498, 164
Kimm T., Cen R., 2014, ApJ, 788, 121
Koekemoer A. M. et al., 2011, ApJS, 197, 36
Kriek M. et al., 2015, ApJS, 218, 15
Kroupa P., Boily C. M., 2002, MNRAS, 336, 1188
Labbé I. et al., 2013, ApJ, 777, L19
Le Fèvre O. et al., 2015, A&A, 576, A79
Llerena M. et al., 2021, A&A, Available at: https://www.aanda.org/component/article?access=doi&doi=10.1051/0004-6361/202141651
Luo B. et al., 2017, ApJS, 228, 2
Ma X., Quataert E., Wetzel A., Hopkins P. F., Faucher-Giguère C.-A., Kereš D., 2020, MNRAS, 498, 2001
Madau P., Fragos T., 2017, ApJ, 840, 39
Magliocchetti M. et al., 2020, MNRAS, 493, 3838
Marchi F. et al., 2017, A&A, 601, A73
Marques-Chaves R., Schaerer D., Álvarez-Márquez J., Colina L., Dessauges-Zavadsky M., Pérez-Fournon I., Saldana-Lopez A., Verhamme A., 2021, MNRAS, 507, 524
Matthee J., Sobral D., Gronke M., Paulino-Afonso A., Stefanon M., Röttgering H., 2018, A&A, 619, A136
Mauerhofer V., Verhamme A., Blaizot J., Garel T., Kimm T., Michel-Dansac L., Rosdahl J., 2021, A&A, 646, A80
McLure R. J. et al., 2018, MNRAS, 479, 25
Meštrić U. et al., 2020, MNRAS, 494, 4986
Meštrić U., Ryan-Weber E. V., Cooke J., Bassett R., Prichard L. J., Rafelski M., 2021, MNRAS, 508, 4443
Meyer R. A., Laporte N., Ellis R. S., Verhamme A., Garel T., 2021, MNRAS, 500, 558
Momcheva I. G. et al., 2016, ApJS, 225, 27
Mostardi R. E., Shapley A. E., Nestor D. B., Steidel C. C., Reddy N. A., Trainor R. F., 2013, ApJ, 779, 65
Mostardi R. E., Shapley A. E., Steidel C. C., Trainor R. F., Reddy N. A., Siana B., 2015, ApJ, 810, 107
Naidu R. P., Forrest B., Oesch P. A., Tran K.-V. H., Holden B. P., 2018, MNRAS, 478, 791
Naidu R. P., Tacchella S., Mason C. A., Bose S., Oesch P. A., Conroy C., 2020, ApJ, 892, 109
Naidu R. P. et al., 2021, MNRAS, Available at: https://ui.adsabs.harvard.edu/abs/2021MNRAS.tmp.3287N/abstract
Nakajima K., Ouchi M., 2014, MNRAS, 442, 900
Nakajima K., Fletcher T., Ellis R. S., Robertson B. E., Iwata I., 2018, MNRAS, 477, 2098
Nakajima K., Ellis R. S., Robertson B. E., Tang M., Stark D. P., 2020, ApJ, 889, 161
Nanayakkara T. et al., 2019, A&A, 624, A89
Nonino M. et al., 2009, ApJS, 183, 244
Oke J. B., Gunn J. E., 1983, ApJ, 266, 713
Paalvast M. et al., 2018, A&A, 618, A40
Pahl A. J., Shapley A., Steidel C. C., Chen Y., Reddy N. A., 2021, MNRAS, 505, 2447
pandas development team T., 2020, pandas-dev/pandas: Pandas. Available at: https://doi.org/10.5281/zenodo.3509134
Pentericci L. et al., 2018, A&A, 616, A174
Pérez F., Granger B. E., 2007, Comput. Sci. Eng., 9, 21
Planck Collaboration XIII 2016a, A&A, 594, A13
Planck Collaboration XIII 2016b, A&A, 596, A108
Reddy N. A. et al., 2018, ApJ, 869, 92
Rivera-Thorsen T. E. et al., 2019, Science, 366, 738
Roberts-Borsani G. W. et al., 2016, ApJ, 823, 143
Robertson B. E. et al., 2013, ApJ, 768, 71
Robertson B. E., Ellis R. S., Furlanetto S. R., Dunlop J. S., 2015, ApJ, 802, L19
Romano M., Grazian A., Giallongo E., Cristiani S., Fontanot F., Boutsia K., Fiore F., Menci N., 2019, A&A, 632, A45
Rutkowski M. J. et al., 2017, ApJ, 841, L27
Santini P. et al., 2017, ApJ, 847, 76
Saxena A. et al., 2020a, MNRAS, 496, 3796
Saxena A. et al., 2020b, A&A, 636, A47
Saxena A. et al., 2021, MNRAS, 505, 4798
Schaerer D., Izotov Y. I., Nakajima K., Worseck G., Chisholm J., Verhamme A., Thuan T. X., de Barros S., 2018, A&A, 616, L14
Schaerer D., Fragos T., Izotov Y. I., 2019, A&A, 622, L10
Senchyna P., Stark D. P., Chevallard J., Charlot S., Jones T., Vidal-García A., 2019, MNRAS, 488, 3492
Shapley A. E., Steidel C. C., Strom A. L., Bogosavljević M., Reddy N. A., Siana B., Mostardi R. E., Rudie G. C., 2016, ApJ, 826, L24
Siana B. et al., 2007, ApJ, 668, 62
Siana B. et al., 2015, ApJ, 804, 17
Smit R. et al., 2015, ApJ, 801, 122
Smith B. M. et al., 2020, ApJ, 897, 41
Stark D. P., 2016, ARA&A, 54, 761
Stark D. P., Schenker M. A., Ellis R., Robertson B., McLure R., Dunlop J., 2013, ApJ, 763, 129
Stasińska G., Izotov Y., Morisset C., Guseva N., 2015, A&A, 576, A83
Steidel C. C., Pettini M., Adelberger K. L., 2001, ApJ, 546, 665
Steidel C. C., Bogosavljević M., Shapley A. E., Reddy N. A., Rudie G. C., Pettini M., Trainor R. F., Strom A. L., 2018, ApJ, 869, 123
Tang M., Stark D. P., Chevallard J., Charlot S., 2019, MNRAS, 489, 2572
Tasca L. A. M. et al., 2017, A&A, 600, A110

Downloaded from https://academic.oup.com/mnras/article/511/1/120/6481640 by guest on 17 March 2023

Taylor M. B., 2005, in Shopbell P., Britton M., Ebert R., eds, ASP Conf. Ser. Vol. 347, Astronomical Data Analysis Software and Systems XIV. Astron. Soc. Pac., San Francisco, p. 29
Trebitsch M., Blaizot J., Rosdahl J., Devriendt J., Slyz A., 2017, MNRAS, 470, 224
Trebitsch M., Volonteri M., Dubois Y., Madau P., 2018, MNRAS, 478, 5607
Urrutia T. et al., 2019, A&A, 624, A141
Vanzella E., Siana B., Cristiani S., Nonino M., 2010, MNRAS, 404, 1672
Vanzella E. et al., 2016a, ApJ, 821, L27
Vanzella E. et al., 2016b, ApJ, 825, 41
Vanzella E. et al., 2018, MNRAS, 476, L15
Vanzella E. et al., 2020, MNRAS, 491, 1093
Vanzella E. et al., 2021, A&A, Available at: https://www.aanda.org/component/article?access=doi&doi=10.1051/0004-6361/202141590
Verhamme A., Orlitová I., Schaerer D., Izotov Y., Worseck G., Thuan T. X., Guseva N., 2017, A&A, 597, A13
Waskom M., the seaborn development team, 2020, mwaskom/seaborn. Available at: https://doi.org/10.5281/zenodo.592845
Wise J. H., Demchenko V. G., Halicek M. T., Norman M. L., Turk M. J., Abel T., Smith B. D., 2014, MNRAS, 442, 2560
Yoo T., Kimm T., Rosdahl J., 2020, MNRAS, 499, 5175
Zackrisson E., Inoue A. K., Jensen H., 2013, ApJ, 777, 39

APPENDIX A: LYC AND *HST* CUTOUT GALLERIES WITH BEST-FITTING SEDS OF CANDIDATE LYC LEAKERS

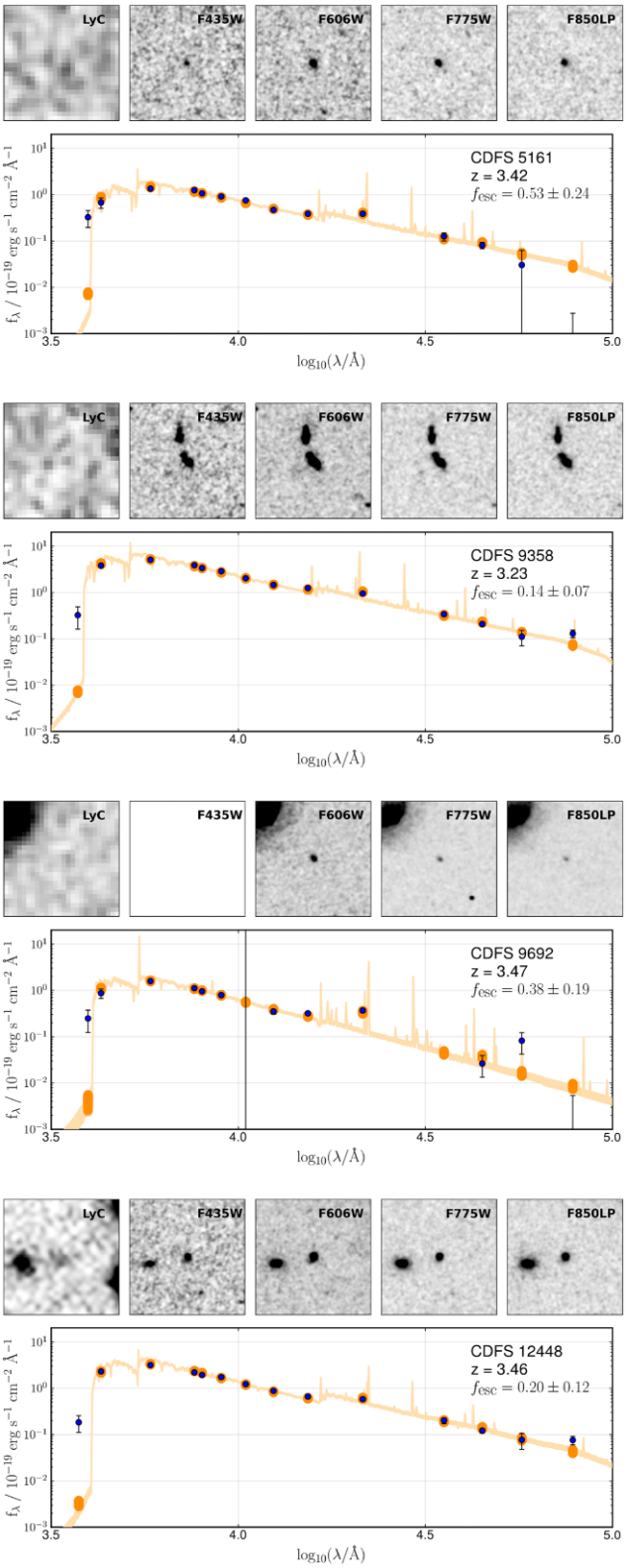
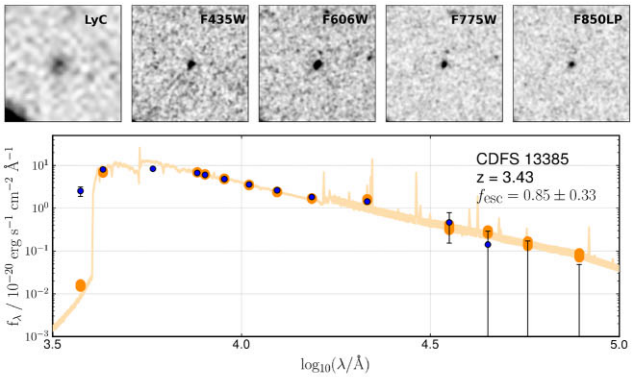
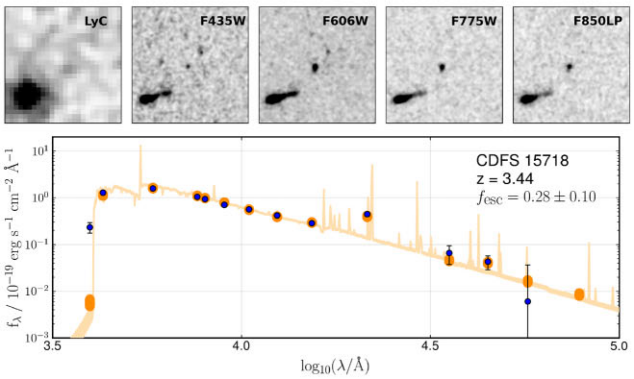
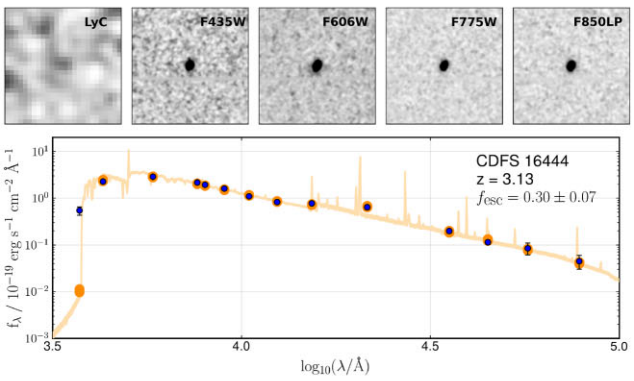


Figure A1. LyC and *HST* photometry (top), and best-fitting SED (orange) with observed (blue points) and SED derived (orange ovals) for candidate LyC leaking galaxies. We show the observed and SED predicted flux at LyC wavelengths only for demonstration purposes – the SED derived LyC fluxes were not used to infer f_{esc} and the observed LyC fluxes were not used during SED fitting to obtain galaxy physical properties.

Downloaded from https://academic.oup.com/mnras/article/511/1/120/6481640 by guest on 17 March 2023







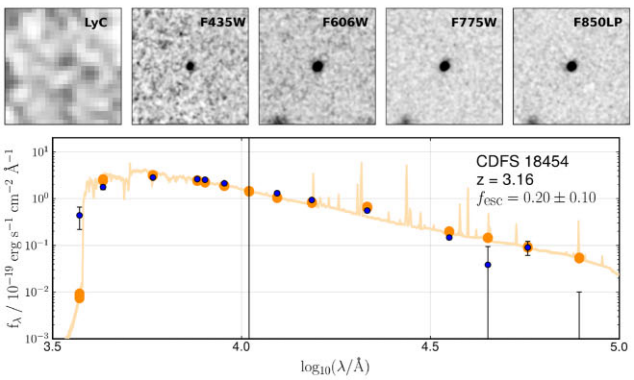
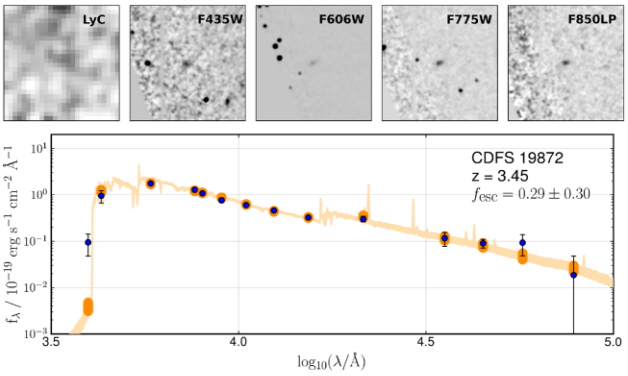
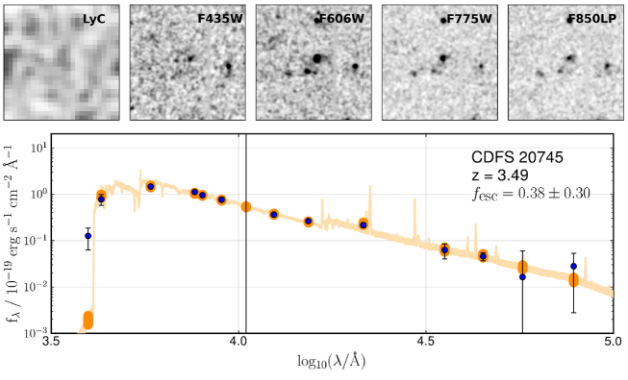


Figure A1. *continued.*





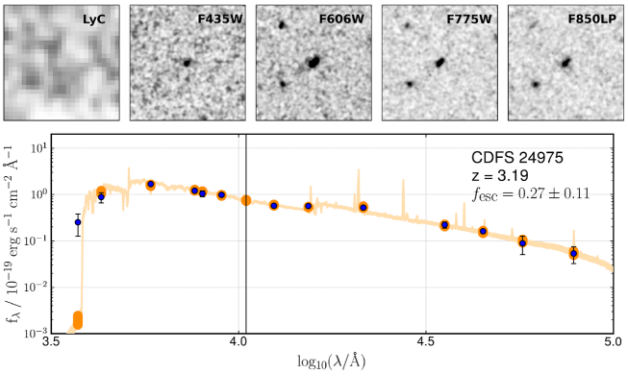


Figure A1. *continued.*

This paper has been typeset from a TEX/LATEX file prepared by the author.

Downloaded from https://academic.oup.com/mnras/article/511/1/120/6481640 by guest on 17 March 2023